NeuroImage 85 (2014) 92–103

Contents lists available at ScienceDirect

NeuroImage

journal homepage: www.elsevier.com/locate/ynimg

Review

Spatial registration for functional near-infrared spectroscopy: From channel position on the scalp to cortical location in individual and group analyses☆

Daisuke Tsuzuki *, Ippeita Dan *

Functional Brain Science Laboratory, Jichi Medical University, 3311-1 Yakushiji, Shimotsuke, Tochigi 329-0498, Japan
Applied Cognitive Neuroscience Laboratory, Research and Development Initiatives, Chuo University, 1-13-27 Kasuga, Bunkyo-ward, Tokyo 112-8551, Japan

ARTICLE INFO

Article history:
Accepted 4 July 2013
Available online 25 July 2013

Keywords:
Optical topography
International 10–20 system
Normalization
Talairach system
Stereotactic coordinate system
3D-digitizer

ABSTRACT

Functional near-infrared spectroscopy (fNIRS) has now become widely accepted as a common functional imaging modality. In order for fNIRS to achieve genuine neuroimaging citizenship, it would ideally be equipped with functional and structural image analyses. However, fNIRS measures cortical activities from the head surface without anatomical information of the object being measured. In this review article, we will present a methodological overview of spatial registration of fNIRS data to overcome this technical drawback of fNIRS. We first introduce and explore the use of standard stereotaxic space and anatomical labeling. Second, we explain different ways of describing scalp landmarks using 10–20 based systems. Third, we describe the simplest case of fNIRS data co-registration to a subject's own MRI. Fourth, we extend the concept to fNIRS data registration of group data. Fifth, we describe probabilistic registration methods, which use a reference-MRI database instead of a subject's own MRIs, and thus enable MRI-free registration for standalone fNIRS data. Sixth, we further extend the concept of probabilistic registration to three-dimensional image reconstruction in diffuse optical tomography. Seventh, we describe a 3D-digitizer-free method for the virtual registration of fNIRS data. Eighth, we provide practical guidance on how these techniques are implemented in software. Finally, we provide information on current resources and limitations for spatial registration of child and infant data. Through these technical descriptions, we stress the importance of presenting fNIRS data on a common platform to facilitate both intra- and inter-modal data sharing among the neuroimaging community.

Contents

Introduction . . . 93
Standard stereotaxic coordinate system . . . 93
Methods for describing scalp positions . . . 95
Registration of fNIRS data to a subject's own structural image . . . 95
Group analyses with direct co-registration to MRI . . . 96
Probabilistic registration for standalone fNIRS data . . . 98
Application of probabilistic registration to DOT . . . 99
Virtual registration . . . 100
Implementation of probabilistic registration in software packages . . . 100
Registration of infant and child data . . . 101
Concluding remarks . . . 102
Acknowledgments . . . 102
References . . . 102

* Corresponding authors at: Functional Brain Science Laboratory, Jichi Medical University, 3311-1 Yakushiji, Shimotsuke, Tochigi 329-0498, Japan.
E-mail addresses: tsuzukid@tamacc.chuo-u.ac.jp (D. Tsuzuki), dan@jichi.ac.jp (I. Dan).

1053-8119/$ – see front matter © 2013 The Authors. Published by Elsevier Inc. All rights reserved.
http://dx.doi.org/10.1016/j.neuroimage.2013.07.025

Introduction

Brain function and brain structure are intrinsically linked to each other. Whether one's interests lie in the function of a particular cortical region or functional network in a certain mental state, the function is described in reference to structure. Together, structural and functional images form the indispensable two wheels of human neuroimaging, and they should be linked through a process called registration (reviewed in Gholipour et al., 2007). While this is also applicable to functional near-infrared spectroscopy (fNIRS), fNIRS poses a distinct problem: the unavailability of structural information.

fNIRS typically measures relative hemoglobin signal changes to estimate cortical hemodynamics or the oxygenation state of cortical tissues, or sometimes cytochrome oxidase activity to estimate cortical metabolic state (reviewed in Obrig and Villringer, 2003). The basic concept of fNIRS for monitoring the hemodynamics of human tissue was first presented by Jobsis (1977). Later, the near-infrared technique was applied to measure hemodynamics associated with functional cortical activity in the early 1990s (Chance et al., 1993; Hoshi and Tamura, 1993; Kato et al., 1993; Villringer et al., 1993), representing the advent of fNIRS (reviewed in Ferrari and Quaresima, 2012).

In these early days, the number of source–detector probe pairs, or channels, was limited to one, or at most a few channels distantly placed to avoid light interference. Multichannel fNIRS instruments were then developed with an array of multiple source–detector pairs that allowed simultaneous monitoring across brain regions (Maki et al., 1995). Multichannel fNIRS data are often treated in a discrete manner, and subjected to channel-wise statistical analysis within a subject (e.g., Schroeter et al., 2002) or among a group of subjects (e.g., Okamoto et al., 2004b). To form spatially continuous functional images, these multichannel fNIRS data have been transformed via spatial interpolation to generate two-dimensional topographic images of brain activation (Maki et al., 1995). Moreover, when head and brain tissues are segmented, the light propagation from a source to a detector can be simulated (Okada et al., 1997). Accordingly, a continuous image is reconstructed to provide more accurate source estimations using short and long distance measurements to provide depth resolution. The resulting two- or three-dimensional reconstructed images are called diffuse optical imaging (DOI) or diffuse optical tomography (DOT) (Barbour et al., 1995; Bluestone et al., 2001; Boas et al., 2004; Culver et al., 2003; Note: DOI and DOT are usually used interchangeably with the latter favoring three-dimensional imaging).

However, fNIRS data is primarily obtained from the head surface without structural information for the brain. Thus, fNIRS measures brain activation, but cannot identify the source of activation on the cortical structure. In order to spatially assess fNIRS data, we must find the correspondence between the scalp location where an fNIRS measurement is performed, and its underlying cortical surface where the source signal is located. Namely, fNIRS data obtained on the scalp should be registered to its underlying cortical surface.

Hence, in this review article, we will present a methodological overview of spatial registration of fNIRS data. First we introduce and explore the use of standard stereotaxic space and anatomical labeling. Then we explain different ways of describing scalp landmarks using 10–20 based systems. Next, we describe the co-registration of fNIRS data to a subject's own MRI, and extend this to fNIRS data registration of group data. Combining these techniques, we describe probabilistic registration methods, which use a reference-MRI database instead of a subject's own MRIs thus enabling MRI-free registration. Subsequently, we extend the concept of probabilistic registration to three-dimensional (3D) image reconstruction in DOT. Moreover, we describe a 3D-digitizer-free method for the virtual registration of fNIRS data onto the stereotactic brain coordinate system. After presenting this theoretical framework, we provide practical guidance on how these techniques are implemented in software. To introduce an ongoing technical front, we also provide current resources and limitations for the spatial registration of child and infant data. Finally, we discuss the future direction of the spatial registration of fNIRS data.

Standard stereotaxic coordinate system

In group studies, functional data must be integrated across subjects to generate a unified inference. While a functional image can be obtained for individual inference, as for a case study or an individual diagnosis, in many cases inference is made for the population from which the subjects are extracted. However, as functional data are tightly bound to structure, integration should also be performed for structure. This is not a straightforward process, as cortical structures vary across subjects.

In considering fNIRS, let us assume a case where we have multichannel data co-registered to subjects' own MRIs. The problem is that structural MRIs have different shapes and sizes and that the orientations of sulci are as unique as fingerprints. One working solution, long sought by researchers, to cope with such structural variability is to standardize the brain structure to achieve a common anatomical platform (Brett et al., 2002). The first legendary achievement was Brodmann's atlas, in which Brodmann examined the cytochemical architecture of a cerebral cortex, and classified the cortex into approximately 50 different regions for humans (Brodmann, 1908). From the time of its invention, the two-dimensional sketch served as the standard for describing cortical anatomy for 80 years. Next came the advent of the Talairach atlas (Talairach and Tournoux, 1988), which is based on the intensively examined brain of a single subject: an elderly Caucasian woman. Two important features of the atlas are the introduction of the stereotactic coordinate system, which describes major anatomical structures of the brain in common three-dimensional space, and its inclusion of descriptions of all of the Brodmann regions. Even today, this atlas serves as a standard system, mostly because several popular analytical software packages for fMRI, including AFNI (Analysis of Functional Neuroimages), have adopted it as their standard coordinate system (Cox, 1996), with the original coordinates being modified to originate at the anterior commissure and the y axis to pass through the posterior commissure.

One major problem with the Talairach atlas is that it is based on a single subject's brain, and thus the shape and anatomical structures are biased. To compensate for this, an averaged brain template, made by co-registering different brains, is used as an alternative. The most widely used template, called MNI (Montreal Neurological Institute) 152 (also known as ICBM 152, where ICBM stands for International Consortium for Brain Mapping) was created by averaging 152 brains co-registered to the Talairach brain (Collins et al., 1994). MNI152 is a relatively unbiased representative of the gross human brain structure. It is widely used as a standard template for SPM (Statistical Parametric Mapping) (Friston et al., 1994). However, global standardization necessarily entails the loss of anatomical detail. Substantial averaging cancels out individual differences in cortical structures. Consequently, the MNI template has a smooth surface without sulci, except for some traces of Sylvian fissures, but it provides a common space for probabilistic description, thereby allowing us to statistically assess both functional activation and anatomical data (Fig. 1B). For example, specific functional activation data may be bound for a particular voxel [−62, 2, 31] and neighboring voxels, and anatomically this activation focus is most likely located on the left central gyrus. Such inference aiming at generalization is best made possible on an unbiased standard brain to represent the brain anatomy of the general population, rather than a canonical brain based on single subject's anatomy.

Anatomical information in MNI space is most conveniently achieved in reference to the Colin27 standard brain (Fig. 1A), which was made by averaging 27 scans of structural MRIs for an individual normalized to MNI space (Collins et al., 1994; Note: "Colin" is the subject and "Collins" is the author). One useful resource is the automatic anatomical labeling (AAL) tool originally provided as a toolbox for SPM (Tzourio-Mazoyer et al., 2002) (Figs. 1C and 2A, D). AAL presents a complete description

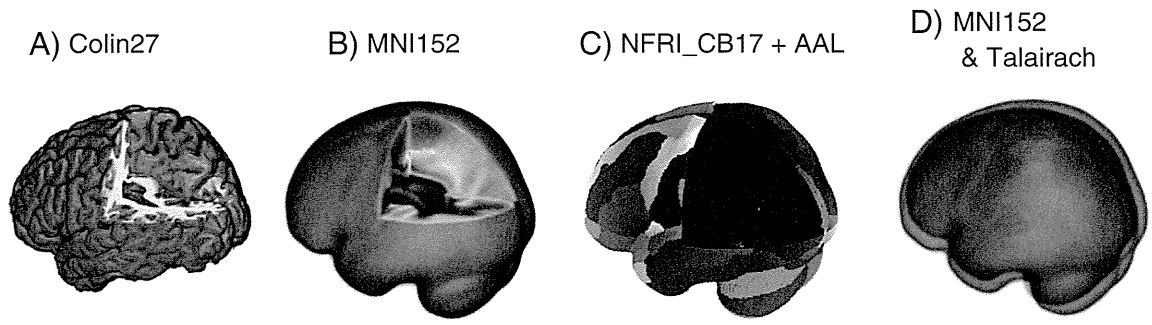

Fig. 1. Comparison among standard brains. All standard brains are aligned in and viewed from the same angle. (A) Colin27 with macro-anatomical information. (B) MNI152 template with smoothed cortical structures due to averaging. (C) NFRI_CB17 (National Food Research Institute Canonical Brain 17) optimized for fNIRS data registration. Cortical surface is compressed to a single layer to form a shell, where additional structural information such as macro-anatomical atlases and 10/20 landmarks may be registered. In this case, a mode-filtered AAL is overlaid. (D) MNI and Talairach templates aligned in the same coordinate system. Although they have similar shapes, the Talairach template is slightly smaller.

of the macro-anatomical structure of the Colin27 brain in terms of x, y, and z co-ordinates, called voxels, in MNI space. AAL returns estimate for a macro-anatomical structure for given MNI coordinates. If the given coordinate is located in areas A, B, and/or C, the AAL tool will produce a list of these areas along with their anatomical labels (Label A, Label B, Label C). A similar resource, called Talairach Daemon, is also available for the Talairach coordinate system (Lancaster et al., 2000). It should be noted here that MNI and Talairach space can be confused with one another; but, while they are similar, they are indeed different (Fig. 1D). Conversion between MNI and Talairach spaces are made in a convenient Matlab toolbox, icbm2tal (Laird et al., 2010; Lancaster et al., 2007).

AAL and Talairach Daemon are limited in that they are based on a single subject's brain, and thus do not deal with anatomical variability across individuals, making them, in a sense, too deterministic. Anatomy is a variable that can be probabilistically presented on the common stereotactic platform. An alternative probabilistic macro-anatomical template, LPBA40, which was created based on 40 subjects with macro-anatomical segmentation at the gyrus level, is available (Shattuck et al., 2008) (Figs. 2B, E). It provides more probabilistic macro-anatomical information in MNI space. Meanwhile MNI152 has undergone an interesting innovation where the original 152 entries have been nonlinearly and iteratively transformed to form an integrated canonical brain with major sulci being preserved (ICBM152NLin; Fonov et al., 2011). While it provides a macroanatomical structure representing the general population, ready for visual inspection, it still lacks resources for macroanatomical labels. If the nonlinear version of MNI152 were equipped with AAL as is Colin27, it could develop into an unbiased canonical brain.

Additionally, a project lead by Zilles, which aims to probabilistically describe cortical anatomy, including histochemical structures, based on multiple postmortem brains in MNI space is underway (Amunts et al., 2007; Zilles and Amunts, 2010). This can be regarded as a probabilistic renewal of Brodmann's atlas in three-dimensional space. Now that the Matlab toolbox enabling probabilistic cytoarchitectonic mapping (Anatomy toolbox) is available for SPM, the fNIRS community can soon benefit from their achievement.

There is another approach to data standardization, called Freesurfer that is currently gaining popularity (Fischl, 2012). This freeware program segments the brain into white and gray matter, unfolds it onto the surface of a sphere, and deforms it to the standard brain-like shape with visible white- and gray-matter patterns. Freesurfer enables an intuitive grasp of the macroanatomical information, at least for an experienced researcher. Since Freesurfer is best appreciated with three-dimensional structural information, it has a high affinity to the DOT technique. Indeed, some pioneering fNIRS studies have adopted Freesurfer-based data presentation (Abdelnour and Huppert, 2010; Cooper et al., 2012), making it another option for standardizing spatial data for fNIRS.

Since most fMRI and PET data are presented in either MNI or Talairach space, fNIRS data are best appreciated when they are presented in these coordinate systems (and possibly in Freesurfer space in the near future).

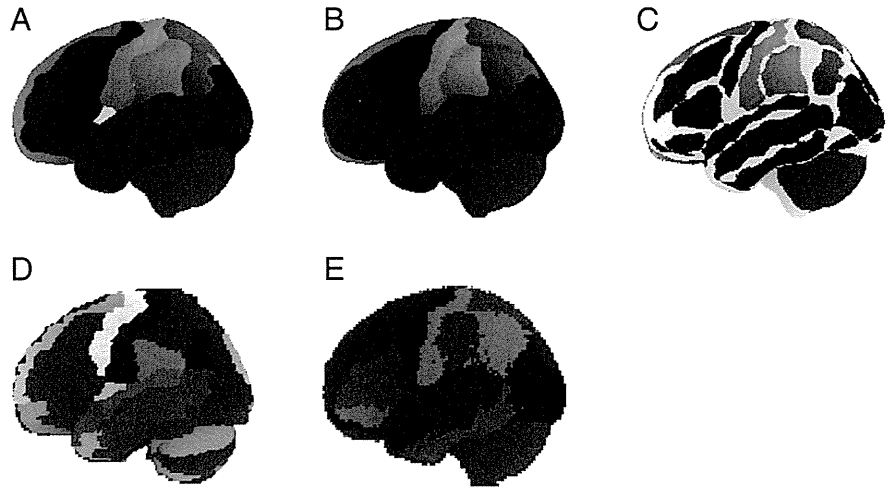

Fig. 2. Comparison between macro-anatomical atlases in MNI space. (A) AAL atlas based on the macro-anatomical segmentation of Colin27 is mode-filtered and projected onto NFRI_CB17 for use of fNIRS spatial registration. Some regions are integrated to maintain compatibility with the macro-anatomical segmentation in LPBA40. (B) LPBA40 atlas based on probabilistic macro-anatomical segmentation of 40 subjects is mode-filtered and projected onto NFRI_CB17 for use of fNIRS spatial registration. (C) AAL and LPBA40 atlases overlapping one another. The commonly labeled regions are depicted in different colors. 64.6% of macro-anatomically labeled voxels (42452/65745) of LPBA40 overlapped with those of AAL, while 69.2% of macro-anatomically labeled voxels (42452/61349) of AAL overlapped with those of LPBA40. (D) Unsmoothed original AAL. (E) Unsmoothed original LPBA40.

Such representation of fNIRS data enables inter-subject, inter-study, and cross-modal comparisons of neuroimaging data. However, it is not yet a common practice to present fNIRS data in these common stereotactic spaces due to the aforementioned technical shortcomings. Therefore, we will describe feasible strategies to address this.

Methods for describing scalp positions

The methods described above require acquisition of a structural image with MRI. However, this is not always guaranteed in typical fNIRS experiments. Even when an MRI is available, its use requires additional cost and effort, reducing the economical merits and convenience of fNIRS. In addition, spatial inference of group fMRI studies is based on a macro-anatomical atlas, and individual MRI scans are mainly used for transformation, not for anatomical inference based on individual cortical structures. Thus, the acquisition of an MRI may not be required for fNIRS group studies since here again MRI is used as a mediator for transformation to the standard brain space.

The fundamental problem of fNIRS in a standalone setting is that fNIRS data is primarily obtained from the head surface without structural information of the underlying brain. Thus, in order to spatially assess standalone fNIRS data, we must find the correspondence between the scalp location where an fNIRS measurement is performed and its underlying cortical surface where the source signal is located: fNIRS data obtained on the scalp should be registered to its underlying cortical surface. The lack of structural information in fNIRS essentially comes down to the issue of cranio-cerebral structural correspondence. Therefore, in a series of studies, we have aimed to solve the fNIRS spatial registration issue by establishing cranio-cerebral correspondence in the modern context of neuroimaging research. Before describing these methods, we will introduce the methods for describing scalp positions.

Currently, the international 10–20 system of electrode placement, which is the recognized standard for scalp electrode positioning for electroencephalography (EEG), is the most prevalent system for positioning electrodes (Jasper, 1958). This system describes scalp locations using relative distances between cranial landmarks with primary landmarks being the nasion (Nz), inion (Iz), and right and left preauricular points (RA, LA) (Supplementary Fig. 1). The 10–20 system then sets landmarks along the scalp systematically at 10% or 20% pitches (Supplementary Fig. 1). The 10–20 system assumes that there is a consistent correspondence between scalp locations and their underlying cerebral structures. Several studies have verified this structural correspondence using cadavers (Blume et al., 1974; Jasper, 1958), X-rays (Morris et al., 1986), CT-scans (Homan et al., 1987; Myslobodsky and Bar-Ziv, 1989; Myslobodsky et al., 1990) and MRIs (Gevins and Illes, 1991; Jack et al., 1990; Lagerlund et al., 1993; Okamoto et al., 2004a; Towle et al., 1993; Van den Elsen and Viergever, 1991).

With the advent of multi-channel EEG hardware systems, and the concurrent development of topographic data visualization methods and sophisticated tomographic signal source localization methods, there was an increased demand for extending the 10–20 system, which defines 21 electrode locations, to a system that allows for a higher-density of electrode settings. Thus, the 10–10 system, which defines 81 electrode locations, was proposed (Chatrian, 1985) (Supplementary Fig. 1). Its modified form has also been accepted as a standard of the American Clinical Neurophysiology Society (ACNS) (American Electroencephalographic Society, 1994; Klem et al., 1999) and the International Federation of Clinical Neurophysiology (IFCN) (Nuwer et al., 1998). Further, Oostenveld and Praamstra logically extended the 10–10 system to the 10–5 system, which has more than 300 electrode locations (Oostenveld and Praamstra, 2001) (Supplementary Fig. 1). For a detailed description of 10–20 and its derivatives, please refer to Jurcak et al. (2007).

Correspondence between 10–20 positions and the underlying macro-anatomical structure was established first by horizontally projecting 10–20 positions onto Brodmann's atlas (Homan et al., 1987). The two-dimensional projection has been extended to a three-dimensional method for 10–20 positions (Okamoto et al., 2004a) and 10–10 positions (Koessler et al., 2009). Meanwhile, correspondence to the MNI coordinate system has been made for 10–20 (Okamoto et al., 2004a) and 10–5 positions (Jurcak et al., 2007). It has been demonstrated that 10–10 positions are separated from one another across the scalp with standard deviations of a dozen mm, while 10–5 positions may be too dense to resolve scalp positions, especially in the occipital regions (Jurcak et al., 2007).

Although the link between scalp landmarks and MNI space are useful in computation, it is intuitively difficult to grasp the correspondence. Cutini et al. (2011) have made a unique contribution towards solving this problem by creating a real MNI152 brain and head model that can be used for fNIRS probe positioning and intuitive real-time mapping simulation by sliding an actual fNIRS probe holder over the physical head model. Although probe design and positioning can be simulated in a digital space, actual deformation of the probe holder and fine adjustments can be better realized on the real head model. This method has yet to be linked to many atlas resources in MNI, but such implementation is relatively easy, especially with the recent spread of 3D printers. Since structural data for standard brains are available on-line, they can be ready for 3D printing after some data conversion using computer-assisted design (CAD) software packages.

Registration of fNIRS data to a subject's own structural image

Regardless of the modality, spatial registration is a fundamental process in neuroimaging. Functional and structural images are obtained differently. For example, an fMRI image is obtained through a protocol called EPI, which takes advantage of the paramagnetic nature of deoxygenated hemoglobin (deoxy-Hb) to capture Blood-Oxygen-Level-Dependent (BOLD) signals (reviewed in Bandettini, 2012). A structural image is obtained as a T1-weighted image that depicts tissues with different fat contents to contrast the gray and white matter of the cortices. They usually have different resolutions, with functional images generally around 5-mm voxels, and structural images around 1 mm (Friston et al., 1996). Both are continuous images consisting of thousands of voxels. Both images are then merged through a process usually called "co-registration", referring to the merging of two or more images (Ashburner and Friston, 1999). This is relatively easy: since the two images are obtained in the same space using the same scanner, the head measurements at different times should match by rigid body transformation. Co-registration produces a functional image of a subject that is visualized over his/her brain.

If a researcher has access to an MRI scanner, a subject's fNIRS data can be co-registered to his/her own structural MRI. This can be executed in several ways, but the essential idea is the same: fNIRS data obtained in a real-world space is merged onto the structural MRI obtained in another real-world space. The most straightforward way to carry this out is to place markers (e.g., vitamin-E capsules or pine-nut beads) to indicate fNIRS probe or channel positions, and take the structural MRI together with these markers (Okamoto et al., 2004a). Then, fNIRS probe or channel positions can be expressed directly on the subject's MRI. Alternatively, fNIRS probe or channel positions are recorded by a three-dimensional (3D) digitizer (typically magnetic) together with the positions of at least three scalp landmarks. The scalp landmarks should be detectable both on the subject's head and on his/her MRI. Technically few points can fulfill this requirement. Therefore, the bilateral preauricular points and the nasion are most often used. Mediated by these landmarks, fNIRS probe or channel locations are transformed to MRI with a rigid body transformation consisting of rotation and translation (Fig. 3).

Once probe/channel locations are described on the real-world space that the subject's MRI belongs to, fNIRS data are either expressed as discrete channel-wise data where functional data (e.g., relative signal change of oxygenated hemoglobin) are bound to channels (Maki et al.,

1995) or a continuous topographic image where a two-dimensional continuous pixel image is created by interpolation (Watanabe et al., 1996). However, since these data are presented on the scalp, not on the cortex, fNIRS data registration goes beyond simple co-registration, and undergoes distinct procedures involving data projection onto the cortical surface (Fig. 3). Projection can be carried out either by searching for the nearest cortical point of a given scalp point, drawing a vertical line from a tangential plane of the scalp point, or drawing a line to a central location such as the centroid of the brain (Okamoto and Dan, 2005). Alternatively, a three-dimensional functional image is reconstructed based on the optical properties of head and brain tissues, and by adopting the photon-measurement density function to each channel consisting of a source–detector pair (Arridge, 1999; Boas and Dale, 2005). Accordingly, signal source distribution is estimated on the subject's MRI with or without depth information in DOT and DOI, respectively (Bluestone et al., 2001; Culver et al., 2003). This method is usually implemented using optional software packages offered by fNIRS constructors. Free software packages such as HomER2, NIRS-SPM and our in-house MATLAB tools are also available for this purpose (Huppert et al., 2009; Ye et al., 2009).

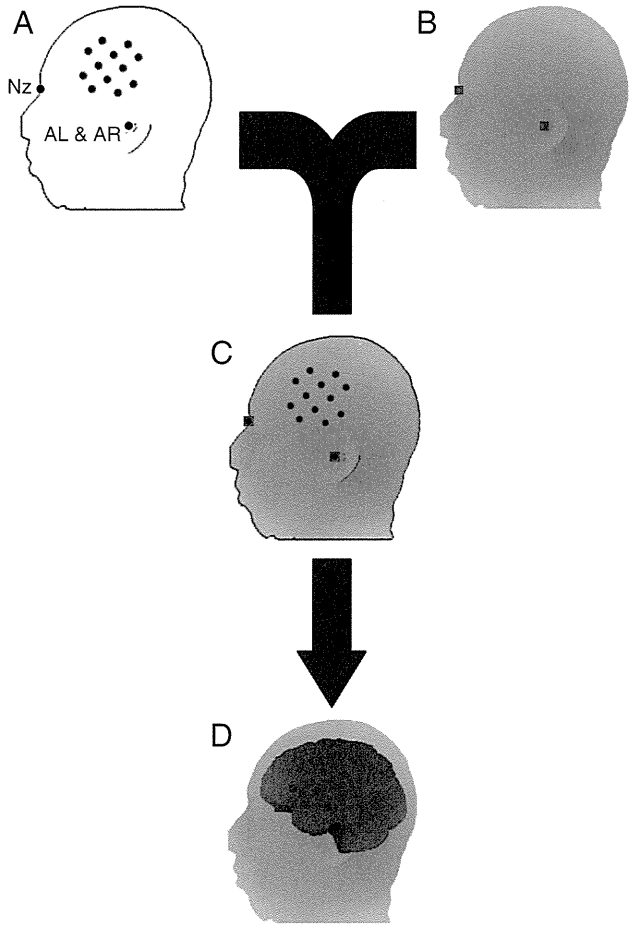

Fig. 3. Registration of channel-wise individual fNIRS data to a subject's own structural image. (A) Multichannel fNIRS channel (blue dots) and reference scalp landmark (black dots) positions on the scalp are measured in a real-world coordinate system using a 3D-digitizer. Nz stands for nasion; AL, left preauricular point; AR, right preauricular point, which is located on the other side of the head. (B) Structural image of the head and brain is obtained using MRI in another real-world coordinate system. The three scalp landmarks (red squares; one on the other side of the head) are also identified manually. (C) The 3D-digitized reference scalp landmarks (black dots) are merged onto the corresponding landmarks on the MRI using rigid-body transformation: thereby, fNIRS positions are also transformed and co-registered onto the subject's own MRI. (D) Finally, the fNIRS channels on the scalp are projected onto the cortical surface (smoothed for better visibility).

Group analyses with direct co-registration to MRI

While a researcher may have a subject's own structural MRI and fNIRS probes/channels co-registered for each subject and can normalize the MRIs to the MNI standard brain, expressing group fNIRS data in the standard brain is not straightforward. For channel-wise analyses, once real-world coordinates of the channels and probes compatible to the structural MRI are available, we would like to report them in the MNI coordinate system. Since normalization is optimized for fMRI, we must perform additional steps to do this (Fig. 4). First, we spatially normalize each subject's MRI head image to the MNI standard brain template using SPM and extract the inverse deformation field matrices. These matrices are used for normalizing the subject's head images from the pre-processing report produced by SPM (Singh et al., 2005). Next, we apply these inverse deformation field matrices to the fNIRS probe and channel positions, and their cortical projections, in order to obtain their coordinate values in MNI space (Tsuzuki et al., 2012). The toolboxes for these procedures are available on our website (http://www.jichi.ac.jp/brainlab/tools.html).

Subsequently, each channel position across subjects in MNI space is averaged to yield the most likely MNI coordinate values (Fig. 5). However, we must be mindful that transformation of a specific scalp/cortical point to the standard brain space entails an error factor intrinsic to transformation. For example, F3 is regarded as the same scalp position across subjects while the cortical projection point for F3 may be transferred to a point with MNI coordinate values of [−35, 49, 32] in one subject but to a nearby point with different coordinate values in another subject. Thus, variability intrinsically associated with spatial transformation should be addressed. Specifically, variability statistics such as standard deviation (SD) along the x, y, and z axes or composite SD (cSD) in terms of radius describes how stable the estimation is (Okamoto et al., 2004a; Singh et al., 2005). In typical multi-channel measurements in adults, cSD is several to a dozen or so mm. Therefore, for a typical fNIRS channel density that does not provide overlapping measurements, distinct channels can be associated fairly well with, for example, a single cortical gyrus or with the Brodmann area.

Here we must reconsider the prerequisite of channel-wise analyses in group studies: channel locations can be considered similar across subjects. As long as the set of probes is small enough and reproducibly placed across subjects, each channel should represent a distinct location on the brain, and thus the spatial identity of a channel is preserved.

However, the independence of a channel is not always guaranteed. With more channels, placement is less reproducible because of variability in head shape and size. An extreme case can be found in whole-head measurement (Koizumi et al., 2003), where the spatial identity of a channel is no longer maintained. In such cases, multi-channel data may be integrated into a region of interest (ROI) (Yanagisawa et al., 2010). For example, if three channels are expected to be located over the left angular gyrus in subject 1, four in subject 2, and two in subject 3, they are respectively grouped to represent the left angular region of each subject (Okamoto et al., 2009). This is also realistic for reproducible channel-wise data because we are not necessarily interested in the functions of channels that are arbitrarily set, but rather in those of macro-anatomical regions.

However, we may have to consider how valid macro-anatomy in a group study is. Even with fMRI, where the macro-anatomical features of each subject are obtained and preserved in MNI space, macro-anatomical information is lost during averaging among subjects. In general, once functional data is expressed in MNI space, macro-anatomical information is regained in reference to anatomical atlases, such as AAL, compatible with MNI space. However, we must remember that AAL is based on the macro-anatomy of a single subject, meaning that functional inferences bound to macro-anatomy in most fMRI studies are based on the particular macro-anatomical structure of that subject. This is an often-neglected reality of fMRI analyses. Nevertheless, here again we are usually interested in functional characteristics of a certain macro-

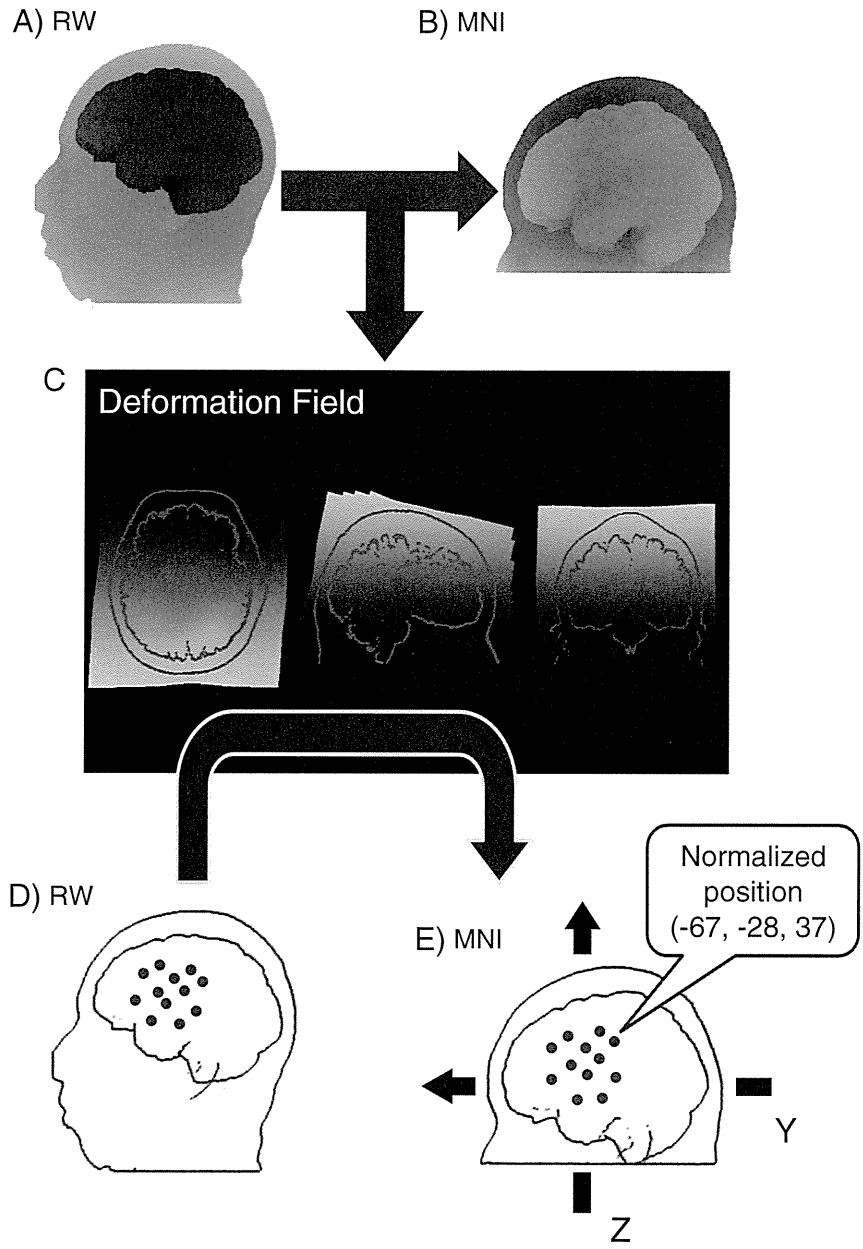

Fig. 4. Normalization of channel-wise individual fNIRS data to the standard brain space. A subject's own MRI in a real-world (RW) coordinate system (A) is normalized to the MNI 152 template to be expressed in MNI space (B) using the SPM program. The deformation field that reflects warping transformation matrix from RW to MNI spaces is extracted (C). Discrete fNIRS channel position data in RW space (D) are transformed to MNI space (E) using the deformation field. Eventually, coordinate values of each fNIRS channel are available in MNI space (Matlab toolbox is available at http://www.jichi.ac.jp/brainlab/tools.html).

anatomical structure, and actually, the macro-anatomical structural differences between individually based AAL and multi-subject-based probabilistic LPBA40 are not substantially different (Fig. 2C). In Fig. 2C, the colored island-like patches represent commonly labeled regions and denote core parts of gyri, consisting of two thirds of the lateral cortical surface. The area that appears as the background in this image corresponds to border regions between gyri. Thus, while group analyses of fMRI data for macro-anatomical functional inference seems reasonable, at least at the gyrus level, inference for the sub-gyrus level may be in question.

Returning to fNIRS, we next consider group analyses of continuous image data, which are either obtained though interpolation or image reconstruction (Fig. 6). In fMRI data, since whole-to-whole transformation is carried out from an individual to the standard brain, the size and orientation of the functional data are intrinsically defined by those of the standard template. In continuous fNIRS image data, individual differences in the scalp shape and size lead to different shapes, sizes and orientations of the continuous image data. While center regions of the continuous image are common across subjects, peripheral regions may not overlap among subjects. This is partially resolved in the NIRS-SPM software package (Ye et al., 2009), which can adjust the degree of overlap (e.g., allowing a region where 60% of data overlap). How to handle the overlap requires more study. For now, center regions that are common among all subjects can be conservatively selected.

Another problem involved in continuous image integration in the standard space is effective spatial resolution, which is often referred to as resolution elements (resels) (Nichols, 2012). Typically, a continuous image with a voxel size of 1 mm is created from more sparsely arranged probes at either a fixed distance of typically 3 cm or differential distances of a few to several cm for image reconstruction in DOT/DOI. Currently,

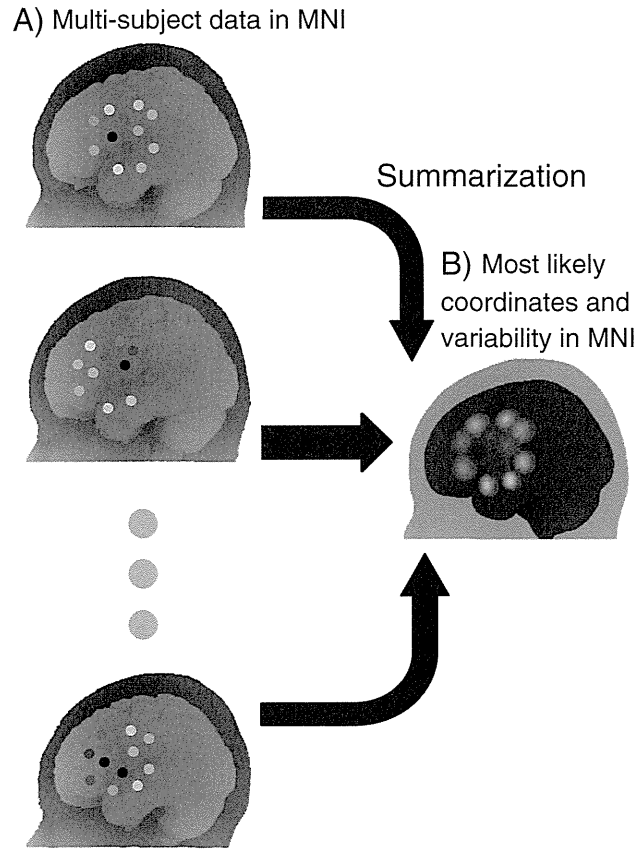

Fig. 5. Integration of channel-wise multi-subject fNIRS data in MNI space. After the process described in Fig. 1, channel-wise fNIRS data for each subject are expressed in MNI space. By repeating this procedure, multi-subject data are available in MNI space (A). They are summarized in MNI space (B), where the coordinates for channel positions are averaged to yield the most likely channel positions (centers of the circles), and variability as expressed in composite standard deviation (radii of the circles). Colors represent activation in a jet scale (red is more activated and green is less activated). Activation patterns are correspondent to those in Fig. 6. Note: this procedure is also applicable for multi-subject data obtained by the probabilistic registration method as described in Fig. 7.

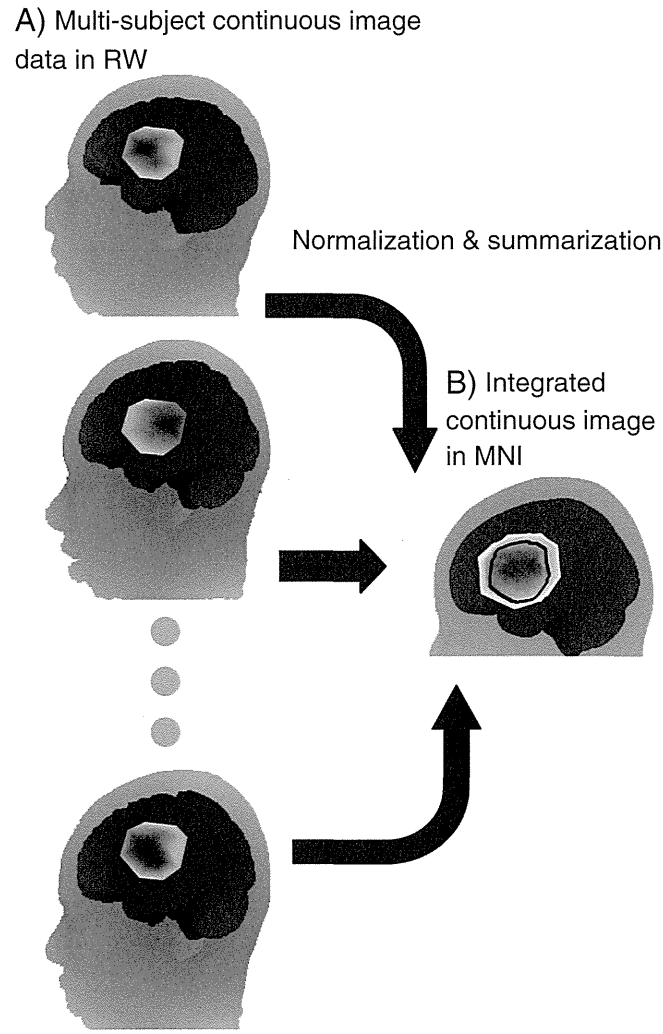

Fig. 6. Integration of continuous image fNIRS data in MNI space. A continuous image is created in a real-world (RW) space for each subject using either interpolation or image reconstruction methods (A). Each image is normalized to MNI space and averaged to one another to yield an integrated continuous image in MNI space (B). The outer edge represents a region that is covered by at least one subject, the inner black boundary represent the region that is covered by all subjects (15 in this simulated data). Colors represent activation in a jet scale (red is more activated and green is less activated). Activation patterns are correspondent to those in Fig. 5.

the finest experimentally resolved resolution of fNIRS data reconstructed in high-density DOT has reached several mm, which is comparable to fMRI resolution (Eggebrecht et al., 2012). However, the effective resolution of typical fNIRS should be greater than that, and, obviously, functional inference at a 1 mm voxel would involve over estimation. Given the currently prevailing convention that functional inference of fMRI group studies is dependent on the resolution of the anatomical labeling tool, functional inference of continuous fNIRS images would also be limited by the same factor.

Robust functional inference for continuous fNIRS image data can be achieved with ROI analyses. One method is to set center coordinate values (e.g., [−67, −26, 30] for the left supra-marginal gyrus), and extract neighboring voxels (e.g., those within 2 cm of the center) to represent a functional status in the ROI. The advantage of this approach is that multiple ROIs of the same size can be set across cortical regions. Note that setting a ROI by integrating channels or voxels is equivalent to applying a spatial filter for smoothing, and thus different ROI sizes result in different degrees of spatial filtering (e.g., the signal to noise ratio of a ROI twice as large as another, can be improved by $\sqrt{2} = 1.4$). Another method is to refer to a macro-anatomical atlas to extract voxels belonging to a given macro-anatomy (e.g., selecting all voxels with the label of right SMG in AAL). This seems a straightforward method, but we should be aware that extreme differences in ROI sizes entail different degrees of spatial smoothing.

Probabilistic registration for standalone fNIRS data

Often the availability of an MR scanner is limited, and even when one is available, mandatory co-use of fNIRS and MRI would reduce the convenience of fNIRS measurements, and impose extra burdens on the subjects. Thus, as a practical alternative, we developed a probabilistic registration method that utilizes MRIs stored in a reference database rather than the subjects' own MRIs, and probabilistically registers fNIRS probe or channel positions onto a standard brain template (Singh et al., 2005) (Fig. 7). We first constructed a reference database containing the head and brain MRIs as well as the 10–20 standard positions of 17 individuals registered to MNI space. This database serves as an anatomical reference in place of a subject's own MRI. We applied an affine transformation of the fNIRS channel coordinates on the subject's head (real-world space), which were obtained with a 3D magnetic digitizer, to the reference heads in the database (MNI space), using 10–20 standard positions as landmarks. Then, we registered head surface points to their corresponding cortical surfaces in MNI space. For group analysis, we obtained a multi-subject distribution of cortical points corresponding to a given fNIRS channel on the head surface. In addition, we obtain the most

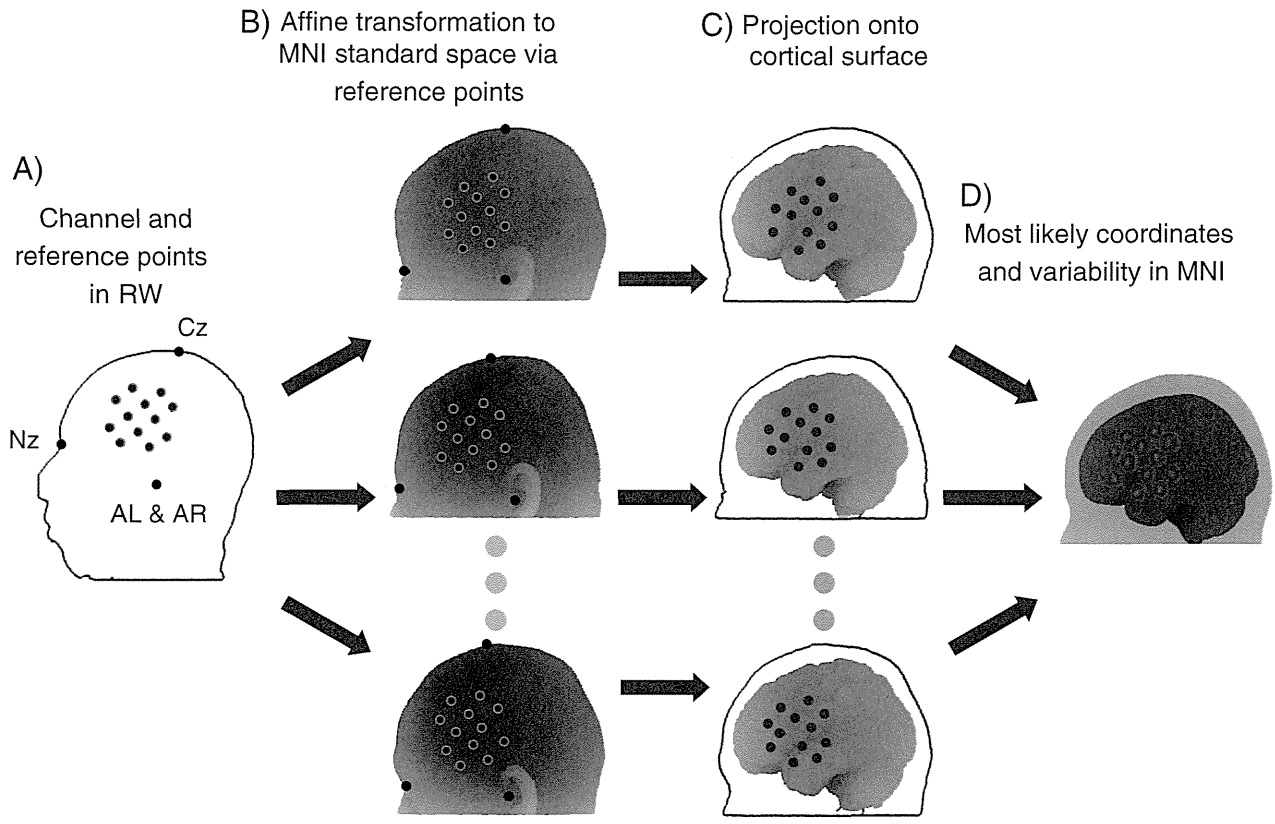

Fig. 7. Probabilistic registration of single-subject data without MRI. (A) Positions for channels and reference points in real-world (RW) space are measured using a 3D-digitizer. The minimum number of reference points is four, as in this case, where Nz (nasion), Cz, and left and right preauricular points (AL and AR) are used. Alternatively, whole or selected 10/20 positions may be used. (B) The reference points in RW are affine-transformed to the corresponding reference points in each entry in reference to the MRI database in MNI space. (C) Channels of the scalp are projected onto the cortical surface of the reference brains. (D) The cortically projected channel positions are integrated to yield the most likely coordinates (average: centers of spheres) and variability (composite standard deviation: radii of spheres) in MNI space. Single-subject data may be subsequently subjected to group analyses as described in Fig. 5.

likely estimate of the cortical point in a group of subjects, as well as cSD representing error effects due to variability across subjects and across reference brains. The cSD of the projected cortical point obtained from the proposed registration process is on the order of millimeters when fNIRS probes are reproducibly set on the scalp (Tsuzuki et al., 2012). This is sufficiently accurate for most functional mapping performed at the gyrus level.

In order to perform probabilistic registration based on affine transformation on three-dimensional space, we need at least four distinct reference landmarks on the scalp. However, a human scalp is not optimized for probabilistic registration. Although three landmarks, most often the Nz and preauricular points, are relatively easy to determine accurately (Jurcak et al., 2007), the fourth position is hard to find and entails considerable variability. The most feasible scalp landmark for realizing a balanced arrangement of the landmarks with sufficient vertical height is Cz of the international 10–20 system. However, determination of Cz is dependent on Iz, leading to ambiguity due to Iz's variability.

Thus, a registration method that avoids Iz and Cz is greatly desirable. To meet this demand, we have introduced an anchor-based probabilistic registration method: a novel method utilizing affine transformation via three distinct cranial landmarks (i.e., Nz and the left and right preauricular points) and an additional anchor point, which can be obtained from anywhere on the scalp (Tsuzuki et al., 2012). The essence of the anchor-based probabilistic registration method lies in its partial use of a spherical coordinate system. Using the three cranial landmarks, we can define a distinct plane from which we can further define a spherical coordinate system. Specifically, we set the midpoint between two preauricular points (AR and AL) as the origin of the spherical coordinate system, and so define the reference plane that passes through this origin toward Nz. Accordingly, transformation from a subject's scalp to a reference head's scalp can be executed in reference to the azimuth and elevation angles. However, the anchor point, transferred to a reference head does not have any link to MNI space. This is solved by extracting the deformation field used for transforming the reference head to MNI space (Ashburner and Friston, 1999; Ashburner et al., 2000;) and using it to transform the anchor point.

Anchor-based probabilistic registration is as stable as conventional probabilistic registration. Comparisons among anchor-based probabilistic registration, conventional probabilistic registration, and SPM-based registration via co-registration to a subject's own MRI revealed that intra- and inter-method variabilities were comparable, with both on the order of millimeters (Tsuzuki et al., 2012). Thus, it is suggested that the absence of a subject's own MRI does not necessarily decrease the accuracy of the spatial registration of fNIRS probes or channels to MNI space in group analyses. In an actual experimental situation, all an experimenter needs to do is to click a 3D-digitizer somewhere on the top of the scalp. This substantially reduces the experimental burden by omitting tedious measurements of Iz and, subsequently, Cz. This method is especially useful in clinical studies where experiment time is often limited.

Application of probabilistic registration to DOT

One promising application of probabilistic registration and its derivatives is the transference of data to DOT, the tomographic variant of fNIRS, which utilizes a relatively large number of sources and detectors to reconstruct 3D images of brain activation (Bluestone et al., 2001; Boas et al., 2003; Culver et al., 2003). DOT uses short and long distance measurements to provide depth resolution and enables separation of superficial scalp signals from deeper brain signals. The spatial resolution

of DOT has been improved to the point where it can construct a detailed retinotopic map in the visual field (Zeff et al., 2007).

However, in order to create a 3D image, DOT generally requires subject-specific spatial priors of the head anatomy that have been segmented into several layers of tissue typically including skin, skull, cerebrospinal fluid, gray matter and white matter (Bamett et al., 2003). This requires a structural MRI of the subject, and the additional segmentation, registration and image reconstruction processes are computationally demanding. This obviously conflicts with the economical merits and convenience of fNIRS. However, this can be solved by applying probabilistic registration methods. Thus, rather than using a subject's own MRI, use of the standard atlas was explored (Custo et al., 2010). Colin27 was selected as the atlas as it is normalized to MNI space and has stable anatomical features so that it can be stably segmented into tissues (Collins et al., 1994). Also, Colin27 is the source of AAL, and thus is optimized for automatic anatomical labeling (Tzourio-Mazoyer et al., 2002). This MRI-free approach to obtaining optical images is based on registering a selected atlas to the subject head surface using probabilistic registration via 10–20 positions and solving the photon migration forward problem on the registered atlas. For the hemodynamic response to median-nerve stimulation, both reconstructed DOT images using the subject-specific brain anatomy and those using the atlas were able to locate the activation focus within the post-central gyrus correctly.

In a subsequent validation study, the diffuse optical images of simulated cortical activation in 4000 distinct regions for 32 subjects were reconstructed using a registered atlas and compared with those obtained using a subject's true anatomy (Cooper et al., 2012). When using a subject-specific MRI, localization error, which is due to diffuse optical image reconstruction, was 9 mm. However, when using a registered atlas, localization error was 18 mm. This error is due to a combination of imperfect registration, anatomical differences between atlas and subject anatomies and the localization error associated with diffuse optical image reconstruction, and thus the cost of using the atlas is 9 mm. The simulated activation had a radius of 10 mm. Since this may be more confined than general activation enrolled in typical cognitive and physical tasks, the localization error may be buried in relatively wide activations. Although a more detailed examination is necessary, it is predicted that atlas-guided DOT would be useful for gyrus-level inference. Given that photon migration simulations in DOT have been accelerated using a GPU-based Monte Carlo algorithm (Fang, 2010), the computational cost of DOT will be less of a problem when the atlas-based technique is used. Thus, we expect that DOT, as well as conventional fNIRS, will benefit from their convenience and economical merits, and acquire a wider range of applications.

Virtual registration

The 3D-digitizer registration methods described above allow the registration of fNIRS channel data onto MNI coordinate space even when a subject's own MRI is not available. However, this system still requires 10–20 landmarks and that the probe positions on a subject's head be carefully measured with a 3D-digitizer in order to reproduce their placement on the MR images of the reference head/brain database. This imposes a certain burden on subjects, and thus limits the application of the probabilistic registration method in some clinical situations. To circumvent this, we have devised a 3D-digitizer-free method for the virtual registration of fNIRS channels onto the stereotactic brain coordinate system (Tsuzuki et al., 2007) (Fig. 8). However, note that this method works only when probe holder positioning and deformation are reproducible across subjects. Essentially, this method allows us to place a virtual probe holder on the scalp by simulating the holder's deformation and by registering probes and channels onto reference brains in place of a subject's brain. First, we constructed a holder deformation algorithm for commercially available probe holders. Next, we simulated the registration of virtual holders on synthetic heads and brains that represent size and shape variations among normal adults. We normalized the registered positions to MNI space. With one thousand repetitions, we statistically estimated the most probable MNI coordinate values together with the errors associated with their estimation. As in the case of the 3D-digitizer method, the standard deviation was on the order of millimeters across the scalp. Thus, the virtual registration method realized the spatial registration of completely stand-alone fNIRS data onto MNI space without using supplementary measures. This method is also applicable for individual data, but the lack of size information can lead to large variability. Thus, for better individual estimation, head size information, such as circumference, would preferably be implemented in simulation (manuscript in preparation).

However, this is based on the careful placement of the probe holder and a detailed examination of the holder shape and deformation. Even a slight deviation in holder shape, such as an insertion of a spacer with a thickness of several millimeters between the holder and the head, may alter the results. Thus, the description of probe settings should be as exact as possible. Although it is automated, the current procedure requires rather complicated parameter settings depending on the types of holders actually used. Thus, we created a virtual registration library for common probe placements in adult subjects, where MNI coordinates and macro-anatomical estimation for fNIRS channels are available.

Implementation of probabilistic registration in software packages

As fNIRS use expands, there is an increasing need for software packages to process the data. Currently there are three major freeware packages that work on Matlab. These packages have adopted probabilistic registration tools and thus can perform spatial registration to MNI space for standalone fNIRS data. We will briefly introduce how these packages utilize probabilistic registration.

First, HomER2 is an integrative fNIRS data processing tool with a user-friendly graphical user interface (GUI). The first version was developed by Huppert et al. (2009), and the most recent version is maintained by Dr. Boas's lab at Massachusetts General Hospital. HomER2 offers an interactive spatial registration interface with 10–20 landmarks preset in a GUI. Users can design probe arrangements virtually with the GUI. HomER2 is compatible with 3D digitizers and thus can perform probabilistic registration for channel-wise analyses and reconstructed continuous images. HomER2 also provides users with "recipes" with which they can define sequences of toolboxes for data processing such as temporal filters, generation of experimental blocks, independent component analyses, GLM, and so on. This allows flexible spatiotemporal data analyses for fNIRS.

Second, NIRS-SPM offers statistical parametric mapping tools for fNIRS (Ye et al., 2009). It generates continuous image data from discrete channel data using inhomogeneous spline interpolation kernels either from individual or group data. When used for standalone fNIRS data, NIRS-SPM transforms the functional image to MNI space using probabilistic registration in reference to 3D digitized data of probe and 10–20 landmark positions. For individual data, it statistically processes time-line data using a regression to basis function with a general liner model (GLM) and adopts Sun's tube formula for adjusting multiple voxel comparison (Sun, 1993; Sun and Loader, 1994). For group analyses, continuous functional images created for each individual are merged together in MNI space and are subjected to second level analyses using a GLM with correction for multiple voxel comparison using the random field theory.

While these two packages offer relatively standardized analytical flow, the final package, Platform for Optical Topography Analysis Tools (POTATo), offers flexible modulation capability upon user demand (Katura et al., 2008). POTATo itself offers no standardized procedures, but provides users with recipes, as does HomER2. The main difference seems to be that POTATo put emphasis on the flexibility of recipes so that new, custom-made functions can be incorporated relatively easily.

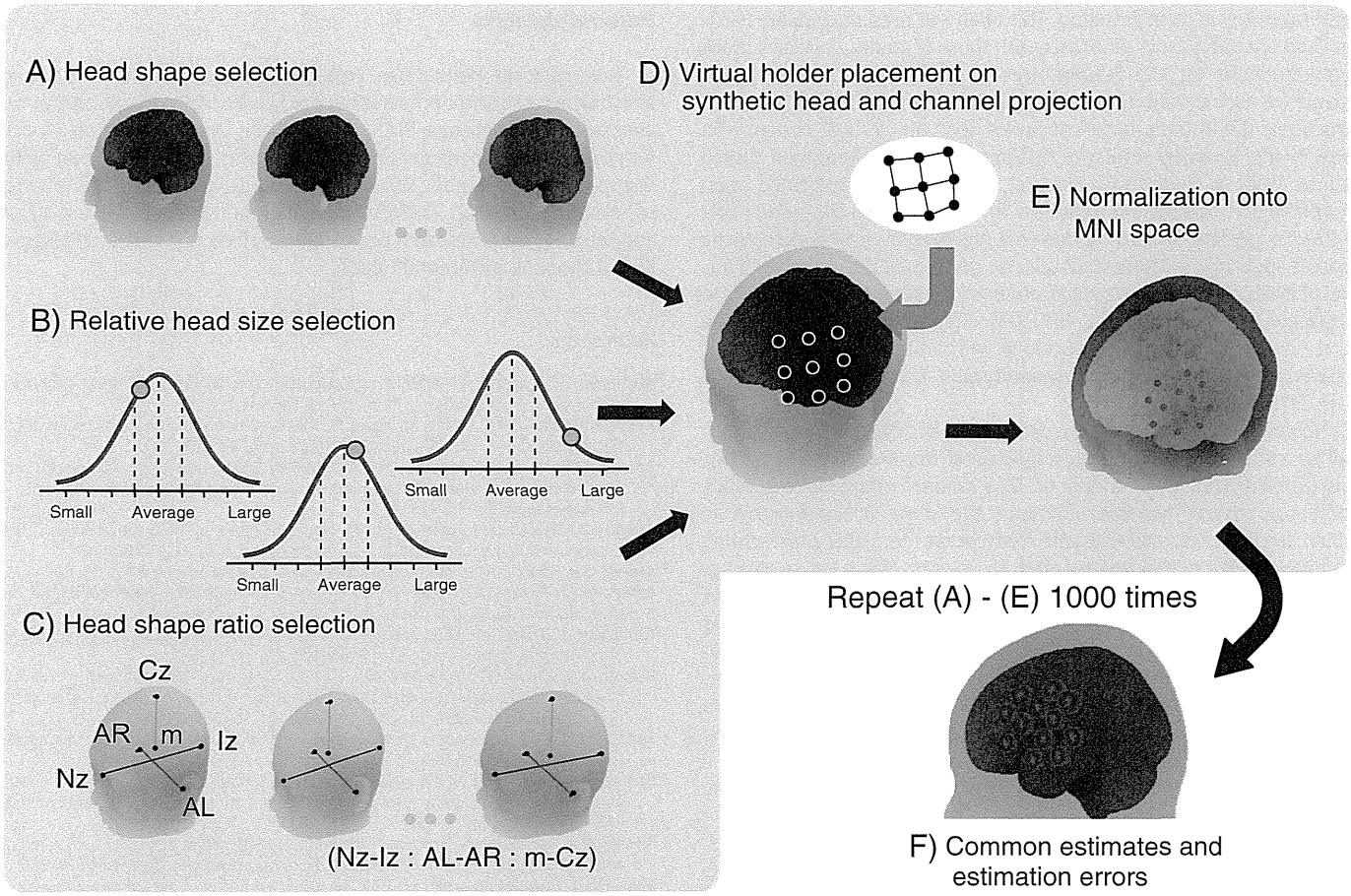

Fig. 8. Virtual registration of multiple-subject data without MRI or a 3D-digitizer. A synthetic head and brain is created from resampling a reference MRI to provide a global head and brain shape (A), relative head size (B), and head shape ratio (C). In (C), m represents the gravity center of AR, AL, Nz and Iz. On the synthetic head, a virtual fNIRS probe holder is placed based on the assumption that probe holder deformation and placement is reproducible (D). From the fNIRS probes (black dots in D), channels are defined as their inter-probe mid points (process not shown). The channels are projected on the synthetic brain and normalized onto MNI space (E). This process is repeated one thousand times to yield the most likely estimates (average: the centers of red circles) and estimation errors (composite standard deviation: the radii of the circles). For a single-subject estimation, the head size in (B) may be fixed to the subject's head size.

Probabilistic registration and virtual registration toolboxes can be incorporated into POTATo in a stable manner (available at http://www.jichi.ac.jp/brainlab/tools.html). Depending on the user's needs, POTATo can process channel-wise data or continuous image data for both individual and group analyses.

Although our toolboxes for probabilistic registrations are available on our website, they are offered as basic Matlab functions with a minimum GUI so that developers can easily integrate them into their own software packages. Relatively experienced users with Matlab literacy may use our native toolboxes, but others may prefer to use them through the software packages introduced above.

Registration of infant and child data

One challenge to be tackled in the near future is the development of registration methods for infant and child fNIRS data. There is no established standard stereotactic system for processing infant brains, but many important initial advances have been made in recent years. The prerequisite for the standard stereotactic system is a probabilistic brain template that can be used for segmentation and normalization, and this was first presented by (Altaye et al., 2008) based on the MRIs of 76 infants at 9 to 15 months old, yielding segmentation of gray matter, white matter and CSF. In addition, the development of age-specific templates has been made for neonates to 4-year-old children (Sanchez et al., 2012), infant brains at any given stage between 29 and 44 gestational weeks (Kuklisova-Murgasova et al., 2011), and 4.5- to 18.5-year-old children (Fonov et al., 2011), allowing segmentation of gray matter, white matter and CSF. Another group has created an average-shape atlas made by aligning 68 neonatal brains to MNI space and averaging them after iterative affine and nonlinear transformation (Shi et al., 2010). Although this atlas included 76 parcellated brain regions, their correspondence to macro-anatomy remains unclear. Macro-anatomical segmentation of neonatal and early infant brains is extremely difficult because only lower contrast images can be obtained compared to adult head scans. Stable macro-anatomical segmentation is only possible from the age of 2: Gousias et al. (2008) succeeded in segmenting 2-year-old brains into 83 regions. While lobe-level macro-anatomical segmentation seems fairly successful, more elaboration is necessary for gyrus-level segmentation.

Reflecting the difficulty of making anatomical atlases specific to infants and young children, extrapolation of an adult atlas to young brains has been implemented as a practical compromise. Shi et al. (2011) created a longitudinal deformation field to transform adult brains to infant brains, through which they projected AAL to neonate, 1-year-old and 2-year-old brains.

We also took a similar approach in our collaboration studies to apply probabilistic or virtual registration procedures to the transformation of scalp fNIRS channels to the cortical template in MNI space based on the assumption that the relative macro-anatomical structural patterns of young infant and child cortices are similar to those of adults. This assumption is based on the study by Hill et al. (2010), which showed that the surface-based atlas of the cerebral cortex in term infants is similar to that of an adult in the pattern of individual variability. Specifically, they have established a population average surface-based atlas of the human

cerebral cortex at term gestation. This atlas was used to compare cortical shape characteristics of infants with those of adults. Cortical surface reconstructions for the hemispheres of 12 healthy term gestation infants were generated from structural MRI data. Based on these reconstructions, the authors have concluded that the cortical structure in term infants is largely similar to that in adults. This assumption should also be valid in children (7–8 years), whose atlas-transformed brain morphology is relatively consistent with that of adults (Burgund et al., 2002). To validate the assumption that registration to MNI stereotactic space is applicable to the infant brain, we performed the virtual registration of fNIRS probe and channel locations of 3- to 6-month-old infants to a neonate AAL atlas (Shi et al., 2011) transformed to MNI space (Altaye et al., 2008). The virtual registrations with adult and neonate brains showed that they are macro-anatomically comparable (Watanabe et al., 2013).

However, this approach is not optimum. Since fNIRS has good potential for cultivating pediatric developmental functional neuroimaging, this problem should be addressed in a manner optimized for fNIRS. There are several possible solutions, the most straightforward of which would be to establish and verify brain templates representing various developmental stages, and to express them in a manner compatible with the MNI coordinate system. As described above, many templates have been produced, but they have different degrees of compatibility with MNI space without satisfactory access to macro-anatomical atlases. Integration of or an inter-link between different systems should be established in the near future. Alternatively, spatial data could be standardized in relative scalp–coordinate systems with direct macro-anatomical links. One plausible solution may be to utilize a spherical coordinate system that was once introduced for standardizing electroencephalography data in the early 90s (Lagerlund et al., 1993; Towle et al., 1993). Also, it would be possible to express scalp and cortical positions via the international 10–20 system or its derivatives. These processes necessarily require manual tracing of macro-anatomical structures at the gyrus level rather than automatic macro-anatomical segmentation. Since macro-anatomical manual tracing for longitudinal volumetry of developmental brains has been implemented in recent years (Tanaka et al., 2012; Uematsu et al., 2012), we can expect substantial progress in the near future.

Concluding remarks

Having undergone two decades of development, fNIRS now seems to be acknowledged among researchers as a feasible neuroimaging modality.This imposes that fNIRS can no longer exist in a vacuum, but should be linked with other imaging modalities to promote brain science. The advent of functional neuroimaging techniques most exemplified by fMRI has revolutionized brain science. Essentially, we can now visualize how the brain regions are activated or connected to each other. However, fMRI measurement constrains subjects in a scanner. Conversely, fNIRS, being compact and allowing more freedom of motion, has the potential to liberate functional neuroimaging from the laboratory into the real world. However, this does not mean the liberation of fNIRS in a methodological context, and isolated development of fNIRS may result in a great loss to the neuroimaging community. Therefore, to facilitate data sharing and cross-referencing among the neuroimaging community, we have devised methods to register spatial fNIRS data onto the common stereotactic brain coordinate systems. By describing fNIRS data on the common stereotactic coordinate systems, we can compare fNIRS data to functional and structural data obtained by other neuroimaging modalities. In turn, fNIRS data can also be referred to by other modalities. We believe such cross-modal interaction of fNIRS is a key factor for promoting the development of fNIRS research, and for furthering neuroimaging research as a whole in the decades to come.

Supplementary data to this article can be found online at http://dx.doi.org/10.1016/j.neuroimage.2013.07.025.

Acknowledgments

We appreciate Haruka Dan, Toshifumi Sano, and Yukie Hirokawa for assisting in manuscript preparation, and Hiroko Ishida for administrative assistance. We appreciate ELCS—English Language Consultation Services for proofreading the manuscript. This work was supported in part by the Grant-in-Aid for Scientific Research from the Japan Society for Promotion of Science (22242012, 23390354, 2370885, and 23650217), and Health and Labor Sciences Research Grants, Research on Psychiatric and Neurological Diseases and Mental Health.

References

Abdelnour, F., Huppert, T., 2010. A random-effects model for group-level analysis of diffuse optical brain imaging. Biomed. Opt. Express 2, 1–25.
Altaye, M., Holland, S.K., Wilke, M., Gaser, C., 2008. Infant brain probability templates for MRI segmentation and normalization. Neuroimage 43, 721–730.
American Electroencephalographic Society, 1994. Guideline thirteen: guidelines for standard electrode position nomenclature. American Electroencephalographic Society. J. Clin. Neurophysiol. 11, 111–113.
Amunts, K., Schleicher, A., Zilles, K., 2007. Cytoarchitecture of the cerebral cortex—more than localization. Neuroimage 37, 1061–1065 (discussion 1066–1068).
Arridge, S.R., 1999. Optical tomography in medical imaging. Inverse Prob. 15, R49–R93.
Ashburner, J., Friston, K.J., 1999. Nonlinear spatial normalization using basis functions. Hum. Brain Mapp. 7, 254–266.
Ashburner, J., Andersson, J.L.R., Friston, K.J., 2000. Image registration using a symmetric prior—in three dimensions. Hum. Brain Mapp. 9, 212–225.
Bamett, A.H., Culver, J.P., Sorensen, A.G., Dale, A., Boas, D.A., 2003. Robust inference of baseline optical properties of the human head with three-dimensional segmentation from magnetic resonance imaging. Appl. Opt. 42, 3095–3108.
Bandettini, P.A., 2012. Twenty years of functional MRI: the science and the stories. Neuroimage 62, 575–588.
Barbour, R.L., Graber, H.L., Jenghwa, C., Barbour, S.L.S., Koo, P.C., Aronson, R., 1995. MRI-guided optical tomography: prospects and computation for a new imaging method. IEEE Comput. Sci. Eng. 2, 63–77.
Bluestone, A., Abdoulaev, G., Schmitz, C., Barbour, R., Hielscher, A., 2001. Three-dimensional optical tomography of hemodynamics in the human head. Opt. Express 9, 272–286.
Blume, W.T., Buza, R.C., Okazaki, H., 1974. Anatomic correlates of the ten-twenty electrode placement system in infants. Electroencephalogr. Clin. Neurophysiol. 36, 303–307.
Boas, D.A., Dale, A.M., 2005. Simulation study of magnetic resonance imaging-guided cortically constrained diffuse optical tomography of human brain function. Appl. Opt. 44, 1957–1968.
Boas, D.A., Strangman, G., Culver, J.P., Hoge, R.D., Jasdzewski, G., Poldrack, R.A., Rosen, B.R., Mandeville, J.B., 2003. Can the cerebral metabolic rate of oxygen be estimated with near-infrared spectroscopy? Phys. Med. Biol. 48, 2405–2418.
Boas, D.A., Dale, A.M., Franceschini, M.A., 2004. Diffuse optical imaging of brain activation: approaches to optimizing image sensitivity, resolution, and accuracy. Neuroimage 23 (Supplement 1), S275–S288.
Brett, M., Johnsrude, I.S., Owen, A.M., 2002. The problem of functional localization in the human brain. Nat. Rev. Neurosci. 3, 243–249.
Brodmann, K., 1908. Beiträge zur histologischen Lokalisation der Großhirnrinde. VI: Die Cortexgliederung des Menschen. J. Psychol. Neurol. X, 231–246 (in German).
Burgund, E.D., Kang, H.C., Kelly, J.E., Buckner, R.L., Snyder, A.Z., Petersen, S.E., Schlaggar, B.L., 2002. The feasibility of a common stereotactic space for children and adults in fMRI studies of development. Neuroimage 17, 184–200.
Chance, B., Zhuang, Z., UnAh, C., Alter, C., Lipton, L., 1993. Cognition-activated low-frequency modulation of light absorption in human brain. Proc. Natl. Acad. Sci. U. S. A. 90, 3770–3774.
Chatrian, G.E., 1985. Ten percent electrode system for topographic studies of spontaneous and evoked EEG activity. Am. J. Electroencephalogr. Technol. 25, 83–92.
Collins, D.L., Neelin, P., Peters, T.M., Evans, A.C., 1994. Automatic 3D intersubject registration of MR volumetric data in standardized Talairach space. J. Comput. Assist. Tomogr. 18, 192–205.
Cooper, R.J., Caffini, M., Dubb, J., Fang, Q., Custo, A., Tsuzuki, D., Fischl, B., Wells III, W., Dan, I., Boas, D.A., 2012. Validating atlas-guided DOT: a comparison of diffuse optical tomography informed by atlas and subject-specific anatomies. Neuroimage 62, 1999–2006.
Cox, R.W., 1996. AFNI: software for analysis and visualization of functional magnetic resonance neuroimages. Comput. Biomed. Res. 29, 162–173.
Culver, J.P., Choe, R., Holboke, M.J., Zubkov, L., Durduran, T., Slemp, A., Ntziachristos, V., Chance, B., Yodh, A.G., 2003. Three-dimensional diffuse optical tomography in the parallel plane transmission geometry: evaluation of a hybrid frequency domain/continuous wave clinical system for breast imaging. Med. Phys. 30, 235–247.
Custo, A., Boas, D.A., Tsuzuki, D., Dan, I., Mesquita, R., Fischl, B., Grimson, W.E., Wells III, W., 2010. Anatomical atlas-guided diffuse optical tomography of brain activation. Neuroimage 49, 561–567.
Cutini, S., Scatturin, P., Zorzi, M., 2011. A new method based on ICBM152 head surface for probe placement in multichannel fNIRS. Neuroimage 54, 919–927.
Eggebrecht, A.T., White, B.R., Ferradal, S.L., Chen, C., Zhan, Y., Snyder, A.Z., Dehghani, H., Culver, J.P., 2012. A quantitative spatial comparison of high-density diffuse optical tomography and fMRI cortical mapping. Neuroimage 61, 1120–1128.
Fang, Q., 2010. Mesh-based Monte Carlo method using fast ray-tracing in Plucker coordinates. Biomed. Opt. Express 1, 165–175.

Ferrari, M., Quaresima, V., 2012. A brief review on the history of human functional near-infrared spectroscopy (fNIRS) development and fields of application. Neuroimage 63, 921–935.
Fischl, B., 2012. FreeSurfer. Neuroimage 62, 774–781.
Fonov, V., Evans, A.C., Botteron, K., Almli, C.R., McKinstry, R.C., Collins, D.L., 2011. Unbiased average age-appropriate atlases for pediatric studies. Neuroimage 54, 313–327.
Friston, K.J., Holmes, A.P., Worsley, K.J., Poline, J.P., Frith, C.D., Frackowiak, R.S.J., 1994. Statistical parametric maps in functional imaging: a general linear approach. Hum. Brain Mapp. 2, 189–210.
Friston, K.J., Holmes, A., Poline, J.B., Price, C.J., Frith, C.D., 1996. Detecting activations in PET and fMRI: levels of inference and power. Neuroimage 4, 223–235.
Gevins, A.S., Illes, J., 1991. Neurocognitive networks of the human brain. Ann. N. Y. Acad. Sci. 620, 22–44.
Gholipour, A., Kehtarnavaz, N., Briggs, R., Devous, M., Gopinath, K., 2007. Brain functional localization: a survey of image registration techniques. IEEE Trans. Med. Imaging 26, 427–451.
Gousias, I.S., Rueckert, D., Heckemann, R.A., Dyet, L.E., Boardman, J.P., Edwards, A.D., Hammers, A., 2008. Automatic segmentation of brain MRIs of 2-year-olds into 83 regions of interest. Neuroimage 40, 672–684.
Hill, J., Dierker, D., Neil, J., Inder, T., Knutsen, A., Harwell, J., Coalson, T., Van Essen, D., 2010. A surface-based analysis of hemispheric asymmetries and folding of cerebral cortex in term-born human infants. J. Neurosci. 30, 2268–2276.
Homan, R.W., Herman, J., Purdy, P., 1987. Cerebral location of international 10–20 system electrode placement. Electroencephalogr. Clin. Neurophysiol. 66, 376–382.
Hoshi, Y., Tamura, M., 1993. Dynamic multichannel near-infrared optical imaging of human brain activity. J. Appl. Physiol. 75, 1842–1846.
Huppert, T.J., Diamond, S.G., Franceschini, M.A., Boas, D.A., 2009. HomER: a review of time-series analysis methods for near-infrared spectroscopy of the brain. Appl. Opt. 48, D280–D298.
Jack Jr., C.R., Marsh, W.R., Hirschorn, K.A., Sharbrough, F.W., Cascino, G.D., Karwoski, R.A., Robb, R.A., 1990. EEG scalp electrode projection onto three-dimensional surface rendered images of the brain. Radiology 176, 413–418.
Jasper, H.H., 1958. The ten-twenty electrode system of the International Federation. Electroencephalogr. Clin. Neurophysiol. 371–375.
Jobsis, F.F., 1977. Noninvasive, infrared monitoring of cerebral and myocardial oxygen sufficiency and circulatory parameters. Science 198, 1264–1267.
Jurcak, V., Tsuzuki, D., Dan, I., 2007. 10/20, 10/10, and 10/5 systems revisited: their validity as relative head-surface-based positioning systems. Neuroimage 34, 1600–1611.
Kato, T., Kamei, A., Takashima, S., Ozaki, T., 1993. Human visual cortical function during photic stimulation monitoring by means of near-infrared spectroscopy. J. Cereb. Blood Flow Metab. 13, 516–520.
Katura, T., Sato, H., Fuchino, Y., Yoshida, T., Atsumori, H., Kiguchi, M., Maki, A., Abe, M., Tanaka, N., 2008. Extracting task-related activation components from optical topography measurement using independent components analysis. J. Biomed. Opt. 13, 054008.
Klem, G.H., Luders, H.O., Jasper, H.H., Elger, C., 1999. The ten-twenty electrode system of the International Federation. The International Federation of Clinical Neurophysiology. Electroencephalogr. Clin. Neurophysiol. Suppl. 52, 3–6.
Koessler, L., Maillard, L., Benhadid, A., Vignal, J.P., Felblinger, J., Vespignani, H., Braun, M., 2009. Automated cortical projection of EEG sensors: anatomical correlation via the international 10–10 system. Neuroimage 46, 64–72.
Koizumi, H., Yamamoto, T., Maki, A., Yamashita, Y., Sato, H., Kawaguchi, H., Ichikawa, N., 2003. Optical topography: practical problems and new applications. Appl. Opt. 42, 3054–3062.
Kuklisova-Murgasova, M., Aljabar, P., Srinivasan, L., Counsell, S.J., Doria, V., Serag, A., Gousias, I.S., Boardman, J.P., Rutherford, M.A., Edwards, A.D., Hajnal, J.V., Rueckert, D., 2011. A dynamic 4D probabilistic atlas of the developing brain. Neuroimage 54, 2750–2763.
Lagerlund, T.D., Sharbrough, F.W., Jack Jr., C.R., Erickson, B.J., Strelow, D.C., Cicora, K.M., Busacker, N.E., 1993. Determination of 10–20 system electrode locations using magnetic resonance image scanning with markers. Electroencephalogr. Clin. Neurophysiol. 86, 7–14.
Laird, A.R., Robinson, J.L., McMillan, K.M., Tordesillas-Gutierrez, D., Moran, S.T., Gonzales, S.M., Ray, K.L., Franklin, C., Glahn, D.C., Fox, P.T., Lancaster, J.L., 2010. Comparison of the disparity between Talairach and MNI coordinates in functional neuroimaging data: validation of the Lancaster transform. Neuroimage 51, 677–683.
Lancaster, J.L., Woldorff, M.G., Parsons, L.M., Liotti, M., Freitas, C.S., Rainey, L., Kochunov, P.V., Nickerson, D., Mikiten, S.A., Fox, P.T., 2000. Automated Talairach atlas labels for functional brain mapping. Hum. Brain Mapp. 10, 120–131.
Lancaster, J.L., Tordesillas-Gutierrez, D., Martinez, M., Salinas, F., Evans, A., Zilles, K., Mazziotta, J.C., Fox, P.T., 2007. Bias between MNI and Talairach coordinates analyzed using the ICBM-152 brain template. Hum. Brain Mapp. 28, 1194–1205.
Maki, A., Yamashita, Y., Ito, Y., Watanabe, E., Mayanagi, Y., Koizumi, H., 1995. Spatial and temporal analysis of human motor activity using noninvasive NIR topography. Med. Phys. 22, 1997–2005.
Morris III, H.H., Luders, H., Lesser, R.P., Dinner, D.S., Klem, G.H., 1986. The value of closely spaced scalp electrodes in the localization of epileptiform foci: a study of 26 patients with complex partial seizures. Electroencephalogr. Clin. Neurophysiol. 63, 107–111.
Myslobodsky, M.S., Bar-Ziv, J., 1989. Locations of occipital EEG electrodes verified by computed tomography. Electroencephalogr. Clin. Neurophysiol. 72, 362–366.
Myslobodsky, M.S., Coppola, R., Bar-Ziv, J., Weinberger, D.R., 1990. Adequacy of the International 10–20 electrode system for computed neurophysiologic topography. J. Clin. Neurophysiol. 7, 507–518.
Nichols, T.E., 2012. Multiple testing corrections, nonparametric methods, and random field theory. Neuroimage 62, 811–815.
Nuwer, M.R., Comi, G., Emerson, R., Fuglsang-Frederiksen, A., Guerit, J.M., Hinrichs, H., Ikeda, A., Luccas, F.J., Rappelsburger, P., 1998. IFCN standards for digital recording of clinical EEG. International Federation of Clinical Neurophysiology. Electroencephalogr. Clin. Neurophysiol. 106, 259–261.
Obrig, H., Villringer, A., 2003. Beyond the visible-imaging the human brain with light. J. Cereb. Blood Flow Metab. 23, 1–18.
Okada, E., Firbank, M., Schweiger, M., Arridge, S.R., Cope, M., Delpy, D.T., 1997. Theoretical and experimental investigation of near-infrared light propagation in a model of the adult head. Appl. Opt. 36, 21–31.
Okamoto, M., Dan, I., 2005. Automated cortical projection of head-surface locations for transcranial functional brain mapping. Neuroimage 26, 18–28.
Okamoto, M., Dan, H., Sakamoto, K., Takeo, K., Shimizu, K., Kohno, S., Oda, I., Isobe, S., Suzuki, T., Kohyama, K., Dan, I., 2004a. Three-dimensional probabilistic anatomical cranio-cerebral correlation via the international 10–20 system oriented for transcranial functional brain mapping. Neuroimage 21, 99–111.
Okamoto, M., Dan, H., Shimizu, K., Takeo, K., Amita, T., Oda, I., Konishi, I., Sakamoto, K., Isobe, S., Suzuki, T., Kohyama, K., Dan, I., 2004b. Multimodal assessment of cortical activation during apple peeling by NIRS and fMRI. Neuroimage 21, 1275–1288.
Okamoto, M., Tsuzuki, D., Clowney, L., Dan, H., Singh, A.K., Dan, I., 2009. Structural atlas-based spatial registration for functional near-infrared spectroscopy enabling inter-study data integration. Clin. Neurophysiol. 120, 1320–1328.
Oostenveld, R., Praamstra, P., 2001. The five percent electrode system for high-resolution EEG and ERP measurements. Clin. Neurophysiol. 112, 713–719.
Sanchez, C.E., Richards, J.E., Almli, C.R., 2012. Neurodevelopmental MRI brain templates for children from 2 weeks to 4 years of age. Dev. Psychobiol. 54, 77–91.
Schroeter, M.L., Zysset, S., Kupka, T., Kruggel, F., Yves von Cramon, D., 2002. Near-infrared spectroscopy can detect brain activity during a color-word matching Stroop task in an event-related design. Hum. Brain Mapp. 17, 61–71.
Shattuck, D.W., Mirza, M., Adisetiyo, V., Hojatkashani, C., Salamon, G., Narr, K.L., Poldrack, R.A., Bilder, R.M., Toga, A.W., 2008. Construction of a 3D probabilistic atlas of human cortical structures. Neuroimage 39, 1064–1080.
Shi, F., Yap, P.T., Fan, Y., Gilmore, J.H., Lin, W., Shen, D., 2010. Construction of multi-region-multi-reference atlases for neonatal brain MRI segmentation. Neuroimage 51, 684–693.
Shi, F., Yap, P.T., Wu, G., Jia, H., Gilmore, J.H., Lin, W., Shen, D., 2011. Infant brain atlases from neonates to 1- and 2-year-olds. PLoS One 6, e18746.
Singh, A.K., Okamoto, M., Dan, H., Jurcak, V., Dan, I., 2005. Spatial registration of multichannel multi-subject fNIRS data to MNI space without MRI. Neuroimage 27, 842–851.
Sun, J., 1993. Tail probabilities of the maxima of Gaussian randomfields. Ann. Probab. 21, 34–71.
Sun, J., Loader, C., 1994. Simultaneous confidence bands for linear regression and smoothing. Ann. Stat. 22, 1328–1345.
Talairach, J., Tournoux, P., 1988. Co-Planar Stereotaxic Atlas of the Human Brain: 3-Dimensional Proportional System: An Approach to Cerebral Imaging. Medical Publishers, New York.
Tanaka, C., Matsui, M., Uematsu, A., Noguchi, K., Miyawaki, T., 2012. Developmental trajectories of the fronto-temporal lobes from infancy to early adulthood in healthy individuals. Dev. Neurosci. 34, 477–487.
Towle, V.L., Bolanos, J., Suarez, D., Tan, K., Grzeszczuk, R., Levin, D.N., Cakmur, R., Frank, S.A., Spire, J.P., 1993. The spatial location of EEG electrodes: locating the best-fitting sphere relative to cortical anatomy. Electroencephalogr. Clin. Neurophysiol. 86, 1–6.
Tsuzuki, D., Jurcak, V., Singh, A.K., Okamoto, M., Watanabe, E., Dan, I., 2007. Virtual spatial registration of stand-alone fNIRS data to MNI space. Neuroimage 34, 1506–1518.
Tsuzuki, D., Cai, D.S., Dan, H., Kyutoku, Y., Fujita, A., Watanabe, E., Dan, I., 2012. Stable and convenient spatial registration of stand-alone NIRS data through anchor-based probabilistic registration. Neurosci. Res. 72, 163–171.
Tzourio-Mazoyer, N., Landeau, B., Papathanassiou, D., Crivello, F., Etard, O., Delcroix, N., Mazoyer, B., Joliot, M., 2002. Automated anatomical labeling of activations in SPM using a macroscopic anatomical parcellation of the MNI MRI single-subject brain. Neuroimage 15, 273–289.
Uematsu, A., Matsui, M., Tanaka, C., Takahashi, T., Noguchi, K., Suzuki, M., Nishijo, H., 2012. Developmental trajectories of amygdala and hippocampus from infancy to early adulthood in healthy individuals. PLoS One 7, e46970.
Van den Elsen, P.A., Viergever, M.A., 1991. Marker guided registration of electromagnetic dipole data with tomographic images. In: Colchester, A.C., Hawkes, D.J. (Eds.), Information Processing in Medical Imaging. Springer, Berlin, pp. 142–154.
Villringer, A., Planck, J., Hock, C., Schleinkofer, L., Dirnagl, U., 1993. Near infrared spectroscopy (NIRS): a new tool to study hemodynamic changes during activation of brain function in human adults. Neurosci. Lett. 154, 101–104.
Watanabe, E., Yamashita, Y., Maki, A., Ito, Y., Koizumi, H., 1996. Non-invasive functional mapping with multi-channel near infra-red spectroscopic topography in humans. Neurosci. Lett. 205, 41–44.
Watanabe, H., Homae, F., Nakano, T., Tsuzuki, D., Enkhtur, L., Nemoto, K., Dan, I., Taga, G., 2013. Effect of auditory input on activations in infant diverse cortical regions during audiovisual processing. Hum. Brain Mapp. 34, 543–565.
Yanagisawa, H., Dan, I., Tsuzuki, D., Kato, M., Okamoto, M., Kyutoku, Y., Soya, H., 2010. Acute moderate exercise elicits increased dorsolateral prefrontal activation and improves cognitive performance with Stroop test. Neuroimage 50, 1702–1710.
Ye, J.C., Tak, S., Jang, K.E., Jung, J., Jang, J., 2009. NIRS-SPM: statistical parametric mapping for near-infrared spectroscopy. Neuroimage 44, 428–447.
Zeff, B.W., White, B.R., Dehghani, H., Schlaggar, B.L., Culver, J.P., 2007. Retinotopic mapping of adult human visual cortex with high-density diffuse optical tomography. Proc. Natl. Acad. Sci. U. S. A. 104, 12169–12174.
Zilles, K., Amunts, K., 2010. Centenary of Brodmann's map—conception and fate. Nat. Rev. Neurosci. 11, 139–145.

NeuroImage: Clinical 4 (2014) 53–63

Contents lists available at ScienceDirect

NeuroImage: Clinical

journal homepage: www.elsevier.com/locate/ynicl

Prefrontal activation during inhibitory control measured by near-infrared spectroscopy for differentiating between autism spectrum disorders and attention deficit hyperactivity disorder in adults ☆

Ayaka Ishii-Takahashi [a,*], Ryu Takizawa [a], Yukika Nishimura [a], Yuki Kawakubo [b], Hitoshi Kuwabara [b], Junko Matsubayashi [a], Kasumi Hamada [a,c], Shiho Okuhata [a,d,e,f], Noriaki Yahata [a], Takashi Igarashi [g], Shingo Kawasaki [g], Hidenori Yamasue [a], Nobumasa Kato [h], Kiyoto Kasai [a], Yukiko Kano [b]

[a] Department of Neuropsychiatry Graduate School of Medicine, The University of Tokyo, Tokyo, Japan
[b] Department of Child Neuropsychiatry Graduate School of Medicine, The University of Tokyo, Tokyo, Japan
[c] Graduate School of Comprehensive Human Science, Graduate Course of Disability Sciences, University of Tsukuba, Ibaraki, Japan
[d] Department of Electrical Engineering, Graduate School of Engineering, Kyoto University, Kyoto, Japan
[e] Japan Society for the Promotion of Science, Tokyo, Japan
[f] National Center for Child Health and Development, Tokyo, Japan
[g] Optical Topography Group, Application Development Office, Hitachi Medical Corporation, Chiba, Japan
[h] Karasuyama Hospital, Showa University School of Medicine, Japan

ARTICLE INFO

Article history:
Received 23 June 2013
Received in revised form 2 October 2013
Accepted 3 October 2013
Available online 26 October 2013

Keywords:
Autism spectrum disorders
Attention deficit hyperactivity disorder
Near-infrared spectroscopy
Inhibitory control
Stop signal task

ABSTRACT

The differential diagnosis of autism spectrum disorders (ASDs) and attention deficit hyperactivity disorder (ADHD) based solely on symptomatic and behavioral assessments can be difficult, even for experts. Thus, the development of a neuroimaging marker that differentiates ASDs from ADHD would be an important contribution to this field. We assessed the differences in prefrontal activation between adults with ASDs and ADHD using an entirely non-invasive and portable neuroimaging tool, near-infrared spectroscopy. This study included 21 drug-naïve adults with ASDs, 19 drug-naïve adults with ADHD, and 21 healthy subjects matched for age, sex, and IQ. Oxygenated hemoglobin concentration changes in the prefrontal cortex were assessed during a stop signal task and a verbal fluency task. During the stop signal task, compared to the control group, the ASDs group exhibited lower activation in a broad prefrontal area, whereas the ADHD group showed underactivation of the right premotor area, right presupplementary motor area, and bilateral dorsolateral prefrontal cortices. Significant differences were observed in the left ventrolateral prefrontal cortex between the ASDs and ADHD groups during the stop signal task. The leave-one-out cross-validation method using mean oxygenated hemoglobin changes yielded a classification accuracy of 81.4% during inhibitory control. These results were task specific, as the brain activation pattern observed during the verbal fluency task did not differentiate the ASDs and ADHD groups significantly. This study therefore provides evidence of a difference in left ventrolateral prefrontal activation during inhibitory control between adults with ASDs and ADHD. Thus, near-infrared spectroscopy may be useful as an auxiliary tool for the differential diagnosis of such developmental disorders.

1. Introduction

The differential diagnosis of the 2 commonest types of neurodevelopmental disorders, autism spectrum disorders (ASDs) and attention deficit hyperactivity disorder (ADHD), can be difficult. ASDs are characterized by impairments in social skills and communication, as well as repetitive interests and activities (American Psychiatric Association, 2000; Stigler et al., 2011). ADHD is characterized by symptoms of inattention, hyperactivity, and impulsivity (American Psychiatric Association, 2000). These conditions often share symptoms of inattention, hyperactivity, impulsivity, and neuropsychological deficits in inhibitory control (Willcutt et al., 2005; Corbett et al., 2009). Thus, misclassification between ASDs and ADHD may occur in clinical settings, particularly in cases of ASDs with comorbid ADHD symptoms. Because the clinical symptoms of high-functioning ASDs and ADHD of adulthood have been modified according to environmental and

* Corresponding author at: Department of Neuropsychiatry, Graduate School of Medicine, The University of Tokyo, 7-3-1 Hongo, Bunkyo-ku, Tokyo 113-8655, Japan. Tel.: +81 3 5800 9263; fax: +81 3 5800 6894.
E-mail address: ayayak-tky@umin.ac.jp (A. Ishii-Takahashi).

2213-1582/$ – see front matter © 2013 The Authors. Published by Elsevier Inc. All rights reserved.
http://dx.doi.org/10.1016/j.nicl.2013.10.002

developmental factors (Nylander et al., 2013; Lehnhardt et al., 2012; Hofvander et al., 2009; Michielsen et al., 2013), it is more difficult to establish a differential diagnosis of ASDs and ADHD in adults.

These misclassifications may lead to a suboptimal treatment strategy. For example, the administration of methylphenidate (MPH), which is a common treatment for childhood ADHD (Whalen et al., 1989; Barkley et al., 2005; Newcorn et al., 2008; Jensen et al., 2007), to children with ASDs and comorbid ADHD symptoms is frequently associated with adverse effects (i.e., social withdrawal, irritability, and stereotypy) severe enough to warrant treatment discontinuation (Autism Network, 2005; Di Martino et al., 2004). Despite the insufficient study of the benefits and adverse effects of MPH in adults with ASDs and ADHD symptoms, MPH is often administered in these cases, even without evidence of its efficacy, because it is the first line of pharmacological treatment for adult ADHD (Kooij et al., 2010; Atkinson and Hollis, 2010). Other treatments are more appropriate for adult ASDs, such as selective serotonin reuptake inhibitors (Williams et al., 2010a), risperidone (McDougle et al., 1998), and cognitive behavioral therapy (White et al., 2009; Lang et al., 2010).

The inhibitory dysfunction observed in the two disorders may have different neurobiological bases, despite similar symptomatic and neuropsychological manifestations.

Stop signal and go/no-go tasks are commonly used tasks to detect inhibitory control in neuroimaging studies. The stop signal task creates a higher load on response inhibition processes compared to the go/no-go task, in that it involves the retraction of a response that has already been triggered by a go signal (Rubia et al., 2001). Go/no-go tasks have a higher load on response selection, due to the a priori knowledge about whether or not to respond to the presentation of specific categorical stimuli (Rubia et al., 2001).

Studies of children with ASDs have revealed no significant differences compared to healthy children in the stop signal task (Ozonoff and Strayer, 1997) but lower performance in the go/no-go task (Happé et al., 2006). Inhibitory motor control as assessed by the stop signal task has been studied extensively in ADHD. The meta-analysis revealed a significant difference in stop latency (stop signal reaction time) between ADHD patients and matched controls in both children and adults (Lijffijt et al., 2005), while children with ADHD had lower performance compared to healthy controls in the go/no-go task (Happé et al., 2006; Raymaekers et al., 2007).

Most previous neuropsychological and neuroimaging studies comparing ADHD with ASDs were performed in children. Neuropsychological studies have found that the ASDs group can have either better (Ozonoff and Jensen, 1999; Geurts et al., 2004; Happé et al., 2006) or poorer (Corbett et al., 2009) inhibitory control than the ADHD group. However, some studies showed little difference in executive function profiles between ADHD and ASDs (Goldberg et al., 2005; Verté et al., 2006). The only neuropsychological study performed in adult patients revealed significant differences between ADHD and ASDs in the Stroop task. However, using the Hayling Sentence Completion Test, which assesses verbal response inhibition, it was found that adults with ADHD did not exhibit more severe impairments compared to those with ASDs (Johnston et al., 2011).

Thus, the development of an inhibitory-task-related neurophysiological index as an auxiliary tool for the differential diagnosis of ASDs and ADHD in adults would be an important contribution to this field. Recent functional magnetic resonance imaging (fMRI) and event-related potential studies have revealed differences between children with ASDs and ADHD (Christakou et al., 2012; Malisza et al., 2011; Kemner et al., 1995; Groen et al., 2008). To date, however, no studies have directly compared adults with ASDs to those with ADHD using functional neuroimaging or neurophysiological indices.

Ideally, a diagnostic index should be developed using a neuroimaging tool that is suitable for application in clinical settings. Near-infrared spectroscopy (NIRS) is an optical neuroimaging technique that allows the non-invasive measurement of changes in the concentrations of oxygenated and deoxygenated hemoglobin ([oxy-Hb] and [deoxy-Hb], respectively), thus reflecting regional cerebral blood volume (Hoshi and Tamura, 1993; Villringer et al., 1993). NIRS is safe and portable and allows the examination of subjects in a natural sitting position. The resolution of NIRS for detecting time-course alterations in brain activation in the prefrontal cortex (PFC) is finer than that of fMRI. Therefore, NIRS could be applied as an auxiliary diagnosis tool in clinical psychiatry.

Our research aim was to determine whether prefrontal NIRS signals recorded during an inhibitory control task differed between adults with ASDs and those with ADHD. In this study, we used a stop signal task (SST) to detect brain activation associated with inhibitory control. We chose the letter version of the verbal fluency task (VFT) as a control index of prefrontal function to test whether the findings were task specific. We hypothesized that adults with ASDs and ADHD would exhibit differential prefrontal NIRS signals during the SST, and that both groups of patients would show activation of the PFC compared to the control group. Further, we hypothesized that during the VFT, both groups would show a similarly reduced activation of the PFC compared to the control group.

2. Materials and methods

2.1. Participants

Twenty-one adults with ASDs, 19 adults with ADHD, and 21 healthy control (HC) subjects participated in the study (Table 1). We recruited 26 adults with ASDs and 25 adults with ADHD from the outpatient clinic at the Department of Neuropsychiatry, University of Tokyo Hospital, Japan, and from community clinics. After recruitment of the patient group, some individuals were recruited in the control group in order to match patients for age, sex, and IQ. As a result, all participating subjects were matched for age, sex, and IQ (Table 1). All subjects gave written informed consent in accordance with the Declaration of Helsinki after a complete explanation of the study. The ethics committee of the University of Tokyo Hospital approved this study (approval no.: 630-6). The diagnoses of ASDs and ADHD were established in accordance with the Diagnostic and Statistical Manual of Mental Disorders, 4th edition (DSM-IV) based on comprehensive clinical assessments performed by at least 2 trained child psychiatrists (YK, HK, and AI). We included participants in this study only when at least 2 of the 3 child psychiatrists had seen patients and given consistent diagnoses. Current and lifetime DSM-IV diagnoses, other than ASDs/ADHD, were ruled out based on a consensus decision using information gained from independent clinical interviews, other available clinical data, and from the Mini-International Neuropsychiatric Interview (MINI). The exclusion criteria for all groups were as follows: full-scale IQ < 70, neurological illness, genetic disorders, traumatic brain injury with any known cognitive consequences or loss of consciousness for more than 5 min, a history of electroconvulsive therapy, a history of treatment with stimulants or other psychiatric medication, alcohol/substance abuse or addiction, bipolar disorder, and schizophrenia. An additional exclusion criterion for the control group was personal history of a psychiatric disease, as assessed using the MINI, or a family history of psychiatric disease among their first-degree relatives.

None of the adults with ASDs or ADHD had been treated with stimulants or other psychiatric medication. In Japan, MPH was approved only for treatment of children with ADHD in 2007, and it cannot be used for treating adult ADHD in Japan. Therefore, MPH cannot be used even for cases with severe ADHD symptoms.

The HC group was also free of medication. To the extent possible, we obtained childhood information from a person who knew the patient in childhood (usually the mother). At the time of the recruitment of the subjects, the usage of the Autism Diagnostic Interview, Revised (ADI-R), Autism Diagnostic Observation Schedule (ADOS), and Conners' Adult ADHD Diagnostic Interview for DSM-IV™ (CAADID) was extremely limited in Japan. Before we finished recruitment, we obtained permission

Table 1
Characteristics and task performance.

	ASDs ($n = 21$)	ADHD ($n = 19$)	HC ($n = 21$)		Comparison		
	Mean (SD)	Mean (SD)	Mean (SD)	*P*	Post-hoc *P*		
					ASDs:HC	ADHD:HC	ASDs:ADHD
Age, years	30.8 (7.2)	30.6 (7.4)	28.8 (5.5)	0.60			
Sex, men/women	8 13	11 8	13 8	0.26			
IQ	105.1 (14.6)	102.6 (16.6)	109.0 (5.6)	0.25			
SST (all trials), %	80.8 (11.6)	78.9 (13.8)	84.9 (9.3)	0.26			
SST (stop trials), %	49.2 (38.4)	56.1 (26.3)	65.6 (23.6)	0.22			
SST (go trials), %	94.3 (7.2)	87.7 (20.2)	92.7 (9.8)	0.27			
MRT (SST), ms	498.0 (102.7)	539.1 (100.4)	558.1 (75.8)	0.11			
VFT, words	16.0 (4.3)	15.5 (4.5)	16.9 (4.4)	0.60			
ASRS	3.2 (1.8)	5.2 (0.8)	1.3 (1.1)	<0.01	<0.01	<0.01	<0.01
WURS	53.1 (23.2)	62.1 (20.0)	17.5 (9.3)	<0.01	<0.01	<0.01	0.39
AQ total score	33.5 (7.9)	27.6 (5.5)	13.4 (4.2)	<0.01	<0.01	<0.01	0.02
GAF	51.8 (13.2)	58.8 (10.7)	84.6 (3.1)	<0.01	<0.01	<0.01	0.45
Subtype	Asperger, 5; PDD NOS, 16	ADHD, 11; ADD, 8					

ASDs, autism spectrum disorders; ADHD, attention deficit hyperactivity disorder; HC, healthy control subjects; Asperger, Asperger syndrome; PDD, pervasive developmental disorder; NOS, pervasive developmental disorder - not otherwise specified; IQ, intelligence quotient; SST, stop signal task; MRT, mean reaction time; VFT, verbal fluency task; ASRS, The World Health Organization (WHO) Adult ADHD Inhibitory-Report Scale; WURS, Wender Utah Rating Scale; AQ, autism spectrum quotient; GAF, Global Assessment of Functioning.

to use the ADI-R, ADOS, and CAADID, which were administered by child psychiatrists and psychologists (HK, YK, and AI) to 6 participants (3 ASDs and 3 ADHD participants). The conventional diagnosis was coincident with the diagnosis obtained using ADI-R, ADOS, and CAADID in these 6 participants.

All participants were self-reported right-handers, as assessed using the Edinburgh score (>70) (Oldfield, 1971). The IQ scores of subjects with ASDs and ADHD were obtained using the Wechsler Adult Intelligence Scale-Revised (WAIS-R), Japanese version. The IQ scores of the HCs were estimated using the Japanese version of the National Adult Reading Test (JART) (Matsuoka et al., 2006). Although the JART can measure IQ accurately in HC participants, the test is problematic for participants with ASDs and ADHD because of the well-known imbalances in their intellectual abilities.

A self-reported screening scale was used to assess ADHD symptoms; the World Health Organization (WHO) Adult ADHD Self-Report Scale (ASRS), which was developed in conjunction with the revision of the WHO Composite International Diagnostic Interview (CIDI) (cutoff >3). The Japanese version of the Wender Utah Rating Scale (WURS), which is a self-reporting instrument that is used to identify childhood tendencies toward ADHD retrospectively (cutoff >46) (Matsumoto et al., 2005), was also used. We used these 2 scales in the ASDs and ADHD groups.

We applied the Autism Spectrum Quotient (AQ), as obtained from a self-reported questionnaire, to quantify autistic symptoms in all participants (Baron-Cohen et al., 2001; Wakabayashi et al., 2006). The AQ comprises 50 questions, with 10 questions assessing each of 5 different areas: social skills, attention switching, attention to detail, communication, and imagination. Scores range from 0 to 50 (cutoff >32).

2.2. Task procedure

Hemoglobin concentration ([Hb]) changes were measured during 2 cognitive activation tasks. Subjects sat on a comfortable chair with their eyes open throughout the NIRS measurements and were instructed to minimize movements such as head movements, strong biting, and eye blinking. The sequence of the following 2 tasks was counterbalanced across the subjects.

2.2.1. SST

The cognitive activation task included a 30 s pre-SST, an 81 s SST, and an 80 s post-SST period (Fig. 1A). We selected the block design for the cognitive activation task. In the pre- and post-SST periods (Fig. 1B), the participants were instructed to indicate the direction of an image of a dog (left or right) by pressing a button as quickly as possible. Participants performed 20 trials during the pre-task period and 30 trials during the post-task period. The mean reaction time was calculated automatically during the pre-task period. The image of a dog was displayed for 0.5 s. Between presentation of the images of dogs, a cross shape was shown for 0.4–1.0 s.

During the SST (Fig. 1C), participants were instructed to respond to the "GO" stimulus as quickly as possible during the "GO" trials, and to try to withhold their response on the "STOP" trials (short beep). "STOP" signals were given under 3 conditions of delay after the "GO" stimulus was presented (ΔT equal to mean reaction time [MRT], MRT − 100 ms, and MRT − 250 ms). We used these 3 conditions of delay to avoid the usual tendency to delay the Go response. The subjects performed 21 "GO" trials and 9 "STOP" trials during the SST. We used the total number of correct responses (the number of correct inhibitions plus the number of correct responses to the direction of the dog) divided by the total number of trials as a measure of task performance. We also used the success rate of stop trials and go trials in SST period as a measure of task performance.

2.2.2. VFT

The VFT, which was presented as described previously (Takizawa et al., 2008, 2009), included a 30 s pre-VFT, a 60 s VFT (letter version), and a 70 s post-VFT period. In the pre- and post-task baseline periods, the subjects were instructed to repeat Japanese vowels (/a/, /i/, /u/, /e/, and /o/) aloud. This was intended to correct the data during the fluency task with regard to activation due to vocalization. During the VFT period, participants were instructed to generate as many Japanese words beginning with a designated syllable as possible. This approach is commonly used in the Japanese letter version of the VFT, as Japanese words inevitably begin with a vowel or a consonant–vowel syllable. The 3 initial syllables (first: /to/, /a/, or /na/; second: /i/, /ki/, or /se/; third: /ta/, /o/, or /ha/) were presented in an order that was counterbalanced among the subjects and changed every 20 s during the 60 s task period, to reduce the time during which the subjects remained silent. The subjects were instructed by an auditory cue at the start and end of the task and when the syllable was changed. The total number of correct words generated during the 60 s activation period was used as a measure of task performance.

2.3. NIRS measurement

Relative [oxy-Hb] and [deoxy-Hb] changes were monitored using a 52-channel NIRS machine (Hitachi ETG-4000) at 2 wavelengths of

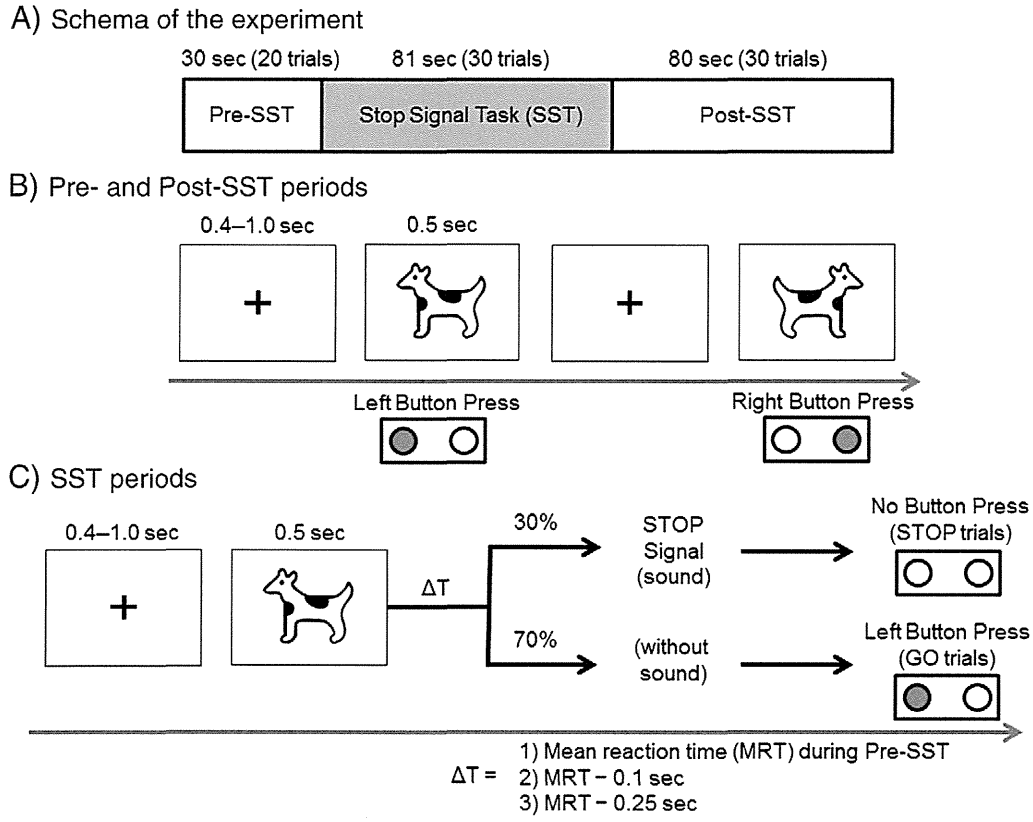

Fig. 1. Schematic representation of the stop signal task. Auditory "STOP" signals were given under 3 conditions of delay (ΔT equal to the mean reaction time [MRT], MRT − 100 ms, and MRT − 250 ms) after the "GO" stimulus was presented.

near-infrared light (695 and 830 nm) based on the modified Beer–Lambert law. The distance between pairs of light source and detector probes was set at 3 cm, and each measurement area between pairs of source/detector probes was defined as a "channel." The probes of the NIRS machine were arranged in 3 × 11 shells and placed on the subject's frontal area. The lowest probes were positioned along the T3–Fpz–T4 line, according to the international 10/20 system. As described previously (Takizawa et al., 2008), this arrangement of the probes is able to detect [Hb] changes in the surface regions of the PFC on bilateral sides (dorsolateral PFC [DLPFC; Brodmann areas (BA) 9 and 46], ventrolateral PFC [VLPFC; BA44, 45, and 47], and frontopolar PFC [; BA10]), and the temporal cortex. To estimate the cortical localization of each channel, we used the virtual registration method (Tsuzuki et al., 2007; Tzourio-Mazoyer et al., 2002), which enables the probabilistic registration of NIRS data onto the Montreal Neurological Institute (MNI) coordinate space without data on magnetic resonance images or probe positions (Fig. 2).

The sampling rate was set to 10 Hz. The pre-task period value was determined as the mean value over a 10 s period just prior to the task period, and the post-task period value was determined as the mean value over the last 10 s of the post-task period. Linear fitting was performed using data from the pre- and post-task periods. The moving average method was used to remove any short-term motion artifacts (moving average window, 5 s). The time resolution of the NIRS apparatus was set at 0.1 s and changes were analyzed using the first-order correction to exclude changes unrelated to the task, such as very slow oscillations or baseline drifts. To acquire a stable baseline, a 20 s non-measured period was included in the 30 s pre-task period; NIRS measurement started in the last 10 s of the pre-task period. Because the NIRS signal was sometimes unstable at the start of the pre-task period, the pre-task baseline was determined as the mean across the last 10 s of the this period, the post-task baseline was determined as the mean across the last 10 s of the post-task period, and a linear fitting was performed on the basis of data between the 2 baselines according to previous NIRS studies (Takizawa et al., 2008; Marumo et al., 2013).

Despite the application of these artifact-rejection methods, visible artifacts sometimes remained in the waveforms. We therefore used a

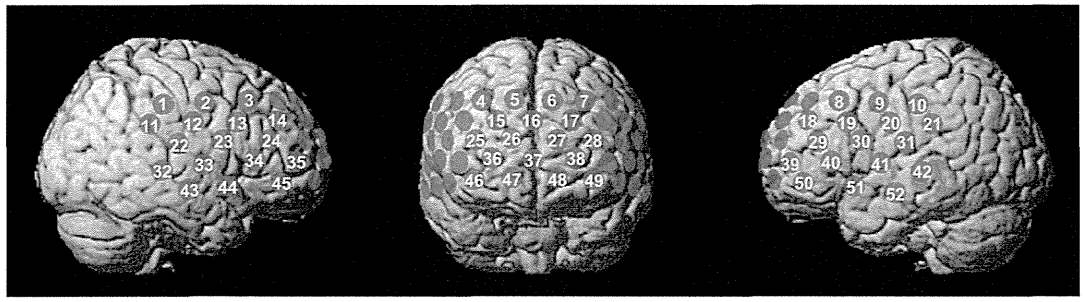

Fig. 2. Locations of the near-infrared spectroscopy (NIRS) probes. The locations of NIRS measurements (channels) were estimated probabilistically and labeled anatomically in the standard brain space (LBPA40) according to Tsuzuki et al. (2007).

computed rejection program (see Inline Supplementary material A.1) that automatically rejected channels that included waveforms with prominent artifacts. Because we excluded the rejected channels from further analyses, the number of available channels varied among individuals.

Finally, the [oxy-Hb] and [deoxy-Hb] data obtained for each channel were averaged for the task period and the [task + post-task] period, respectively. We chose these 2 NIRS signals to detect the time course of [oxy-Hb] and [deoxy-Hb] changes during cognitive tasks.

2.4. Statistical analyses

All statistical analyses were performed using the Statistical Package for the Social Sciences (SPSS) 18 software (SPSS Inc., Tokyo, Japan).

2.4.1. Clinical scale and task performance

Between-group differences in the scores for clinical scales and task performance were tested using a 1-way analysis of variance (ANOVA) and Tukey's honestly significant difference (HSD) test as a post-hoc analysis. A chi-squared test was used for testing sex differences. Clinical and behavioral results were considered significant at $P < 0.05$.

2.4.2. NIRS data

We focused on the mean [oxy-Hb], as the [oxy-Hb] increase is assumed to reflect cognitive activation more directly than does the [deoxy-Hb] decrease, as shown by a stronger correlation of [oxy-Hb] with the blood-oxygenation-level-dependent signal measured by fMRI (Strangman et al., 2002) and by results of animal studies (Hoshi et al., 2001).

For the SST and VFT, mean [oxy-Hb] values were analyzed via one-way ANOVA using the mean [oxy-Hb] as the dependent variable and the diagnosis (ASDs, ADHD, or HC) as the independent variable for each period (the task period or the [task + post-task] period) and for each channel. A false-discovery rate (FDR) correction for multiple comparisons (52 channels) was applied. We set the value for the maximum FDR to 0.05, to allow no more than 5% false positives on average (Singh and Dan, 2006). The mean [oxy-Hb] values were then analyzed using Tukey's HSD test, as a post-hoc analysis, for each period and for each channel.

2.4.3. Classification and cross-validation

The individual expression values were defined as the mean [oxy-Hb] values during the task (or task + post-task) period. We submitted the resulting individual expression values to a parametric Fisher's linear discriminant analysis classification algorithm (Ponseti et al., 2012) in order to discriminate the ASDs from the ADHD group, the ASDs from the HC group, and the ADHD from the HC group.

First, we used stepwise analysis for all channels that showed a significant difference ($P < 0.05$) between the ASDs and ADHD group, the ASDs and HC group, or the ADHD and HC group to select the channels to be used in Fisher's linear discriminant analysis. A stepwise analysis was performed in a forward direction using P values for entry ($P = 0.05$) and removal ($P = 0.10$).

Second, we classified each participant according to these values using Fisher's linear discriminant analysis. We cross validated the classification method using a leave-one-out procedure 40–42 times, to account for each participant. We determined the predictive power of the classification procedure by calculating specificity and sensitivity, as well as average sensitivity and specificity values and mean classification accuracy.

2.4.4. Additional analyses

We evaluated whether [deoxy-Hb] changes had tendencies similar to the [oxy-Hb] changes among the 3 groups, although, overall, we focused on [oxy-Hb] changes. We also addressed prefrontal [oxy-Hb] changes in ASDs adults with ADHD symptoms, who are difficult to differentiate clinically from ADHD adults. We defined a subgroup of ASDs adults who exceeded the ASRS cutoff (>3) ($n = 10$). A different activation between participants with a diagnosis of ASDs who also had ADHD symptoms and the ADHD group would represent an ASDs-specific brain dysfunction. The 3 diagnostic groups (the ASDs subgroup with ADHD symptoms, the entire ADHD group, and the entire HC group) were then compared using the statistical procedures described above. Furthermore, we compared [oxy-Hb] changes between male and female subjects in each group, because a previous NIRS study demonstrated that [oxy-Hb] changes were affected by sex (Kameyama et al., 2004). In addition, we performed a correlation analysis to examine the relationship between [oxy-Hb] changes and clinical conditions and demographic data, such as age, symptom severity, and task performance.

3. Results

3.1. Clinical characteristics and behavioral results

All patients with ADHD and 10 patients with ASDs exceeded the cutoff of the ASRS (Table 1). The ASRS scores of all HC subjects were below the cutoff value. The mean WURS scores of the patients exceeded the threshold (>46), suggesting a difficulty in distinguishing these 2 disorders based on retrospective inhibitory-reporting assessments in their childhood. The ASDs group had significantly higher AQ scores than did the other groups. No statistically significant differences were observed among the 3 groups in any of the task-performance indices.

3.2. NIRS data results

3.2.1. SST

The typical grand-averaged waveforms for [oxy-Hb] in the left VLPFC (ch50) in the HC, ASDs, and ADHD groups are shown in Fig. 3. During the SST period, we found significant main effects of the group in 29 channels (ch1–3, 10–13, 18, 20, 22, 24, 28, 29, 31, 32, 35–39, 41, 42, and 45–51; F [df = 2, 53–58] = 3.911–15.448; FDR-corrected $P \leq 0.001$–0.026).

The [oxy-Hb] changes in the ASDs group were significantly smaller than those in the ADHD group in 2 channels corresponding to the left VLPFC (ch50 and 51; post-hoc $P = 0.030$–0.034) (Figs. 3 and 4, see Inline Supplementary Table S1). Tukey's HSD test indicated that [oxy-Hb] changes in the ASDs group were significantly smaller than those in the HC group in 28 channels corresponding to the bilateral DLPFC, left VLPFC, left premotor area (PMA), left presupplementary motor area (SMA), and frontal pole (ch2, 3, 10–13, 18, 20, 22, 24, 28, 29, 31,

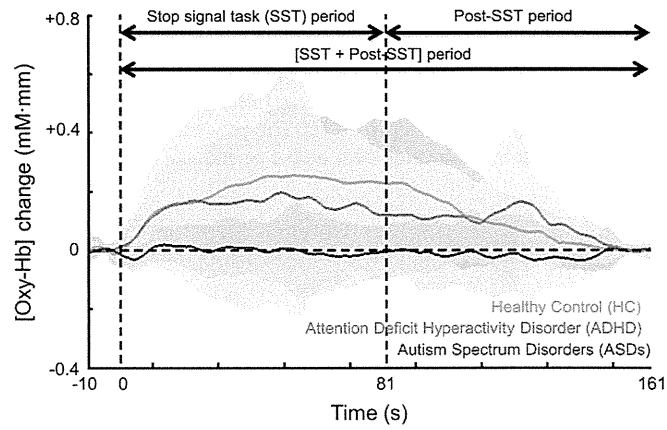

Fig. 3. Time courses of the hemodynamic responses in the left ventrolateral prefrontal cortex (ch50) for the 3 diagnostic groups. The [oxy-Hb] changes for the healthy control (HC) group (black, $n = 21$), attention deficit hyperactivity disorder (ADHD) group (pink, $n = 19$), and autism spectrum disorders (ASDs) group (blue, $n = 21$) during the activation stop signal task (SST) and post-SST conditions are presented as grand-averaged waveforms in ch50. The shaded color indicates the standard deviation.

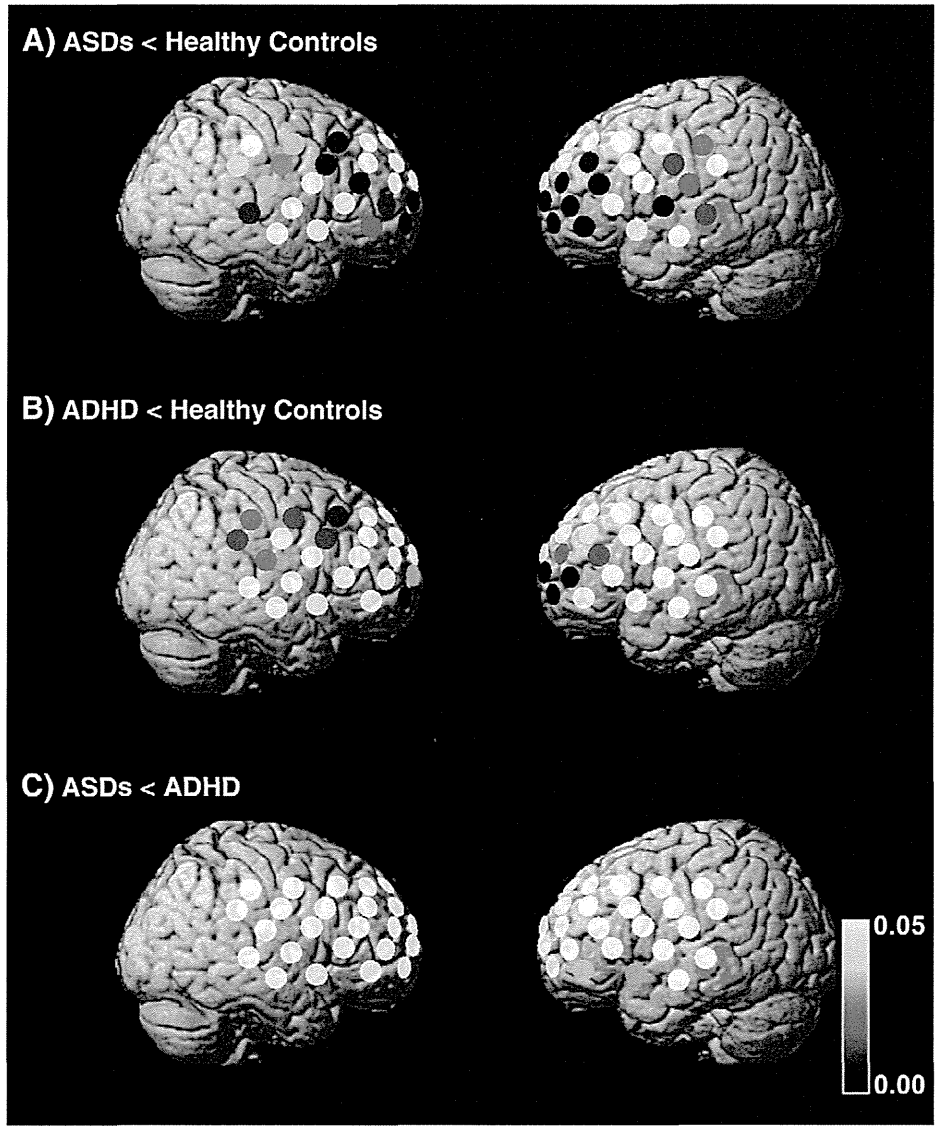

Fig. 4. Differences in [oxy-Hb] changes during the SST between the HC and ADHD groups (A), between the HC and ASDs groups (B), and between the ASDs and ADHD groups (C) (A: post-hoc $P \leq 0.001$–0.046; B: post-hoc $P = 0.001$–0.047: and C: post-hoc $P = 0.030$–0.034). The colored bar represents the P value.

32, 35–39, 41, 42, and 45–51; post-hoc $P \leq 0.001$–0.046) (Figs. 3 and 4, see Inline Supplementary Table S1). [oxy-Hb] changes in the ADHD group were significantly smaller than those in the HC group in 17 channels corresponding to the frontal pole, the bilateral DLPFC, the right PMA, and the right pre-SMA (ch1–3, 11–13, 18, 22, 28, 29, 36, 38, 39, and 46–49; post-hoc $P = 0.001$–0.047) (Fig. 4, see Inline Supplementary Table S1).

Inline Supplementary Table S1 can be found online at http://dx.doi.org/10.1016/j.nicl.2013.10.002.

During the [SST + post-SST] period, there was a main effect of the group in 31 channels (ch2, 3, 8–10, 12, 13, 18, 20, 24, 26–31, 35–39, 41, 42, and 45–52; F [df = 2, 53–58] = 4.291–12.721; FDR-corrected $P \leq 0.001$–0.019).

The [oxy-Hb] increases observed in the ADHD group were significantly larger than those recorded in the ASDs group in 5 channels corresponding to the left VLPFC and frontal pole (ch24, 30, 41, 50, and 51; post-hoc $P = 0.003$–0.046) (Figs. 3 and 5, Supplementary Table A. 2). The number of channels that exhibited significantly different NIRS signals between the ASDs and ADHD groups were larger for the [SST + post SST] analysis than that for the SST analysis, which was mainly driven by a post-SST reascending in [oxy-Hb] in the ADHD group (Fig. 3). The post-hoc Tukey's HSD test revealed that the [oxy-Hb] increases observed during the [SST + post-SST] period in the ASDs group were significantly smaller than those in the HC group in 31 channels corresponding to the bilateral DLPFC, bilateral VLPFC, bilateral PMA, bilateral pre-SMA, and frontal pole (ch2, 3, 8–10, 12, 13, 18, 20, 24, 26–31, 35–39, 41, 42, and 45–52; post-hoc $P \leq 0.001$–0.033) (Figs. 3 and 5, see Inline Supplementary Table S2). The [oxy-Hb] increases observed in the ADHD group were significantly smaller than those in the HC group in 11 channels corresponding to the frontal pole, bilateral DLPFC, right PMA, and right pre-SMA (ch3, 13, 27, 28, 35, 38, 39, and 46–49; post-hoc $P = 0.005$–0.046) (Fig. 5, see Inline Supplementary Table S2).

Inline Supplementary Table S2 can be found online at http://dx.doi.org/10.1016/j.nicl.2013.10.002.

3.2.2. VFT

During the VFT period, we found no significant main effects of the group. There were no significant differences in [oxy-Hb] changes between the ASDs and ADHD groups during the VFT. During the [VFT + post-VFT] period, we found significant main effects of the group in 2 channels (ch13 and 34; F [df = 2, 51–55] = 7.277–8.056; FDR-corrected $P = 0.001$–0.002).

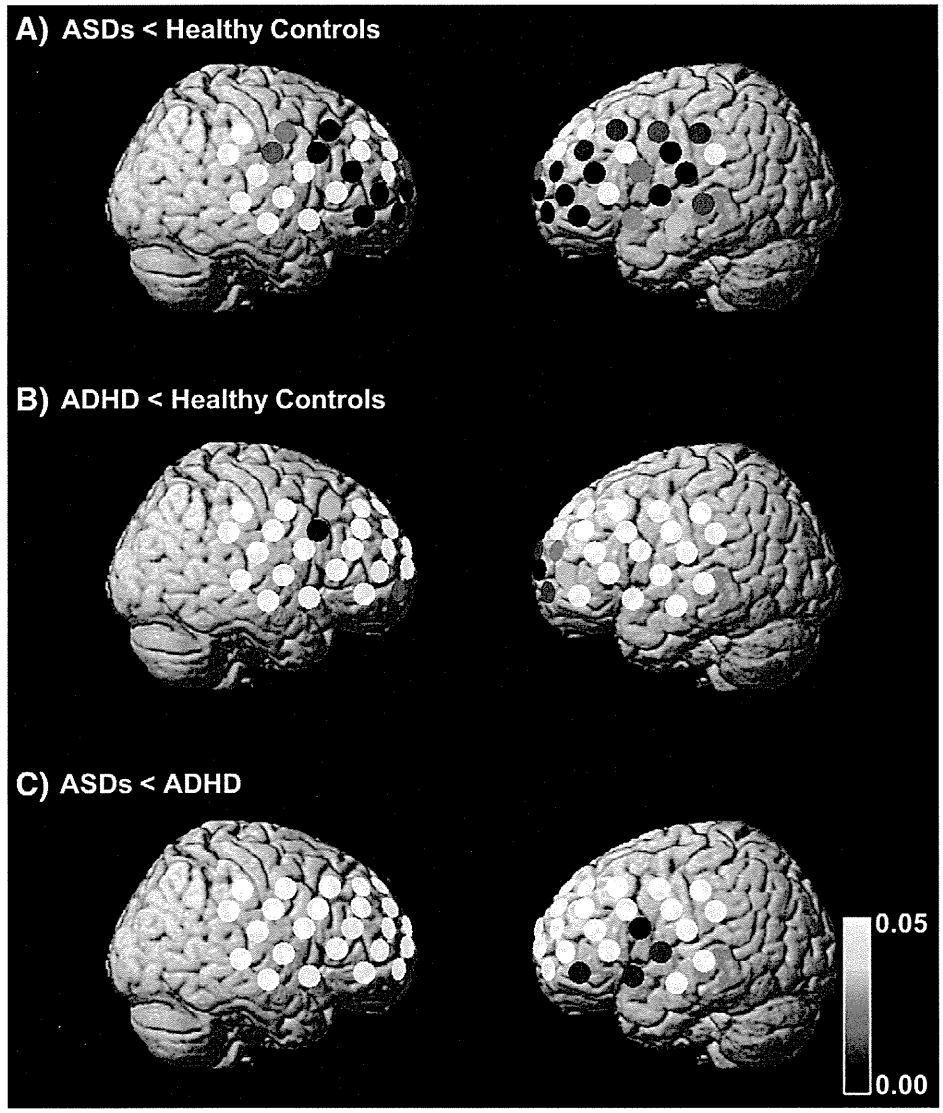

Fig. 5. Differences in [oxy-Hb] changes during the [SST + post-SST] period between the HC and ADHD groups (A), between the HC and ASDs groups (B), and between the ASDs and ADHD groups (C) (A: post-hoc $P \leq 0.001$–0.033; B: post-hoc $P = 0.005$–0.046; and C: post-hoc $P = 0.003$–0.046). The colored bar represents the P value.

There were no significant differences for any channels between the ASDs and ADHD groups during the [VFT + post-VFT] period. Post-hoc Tukey's HSD tests showed that the [oxy-Hb] changes in the ASDs group were significantly smaller than those in the HC group in 2 channels corresponding to the left VLPFC and DLPFC (ch13 and 34; post-hoc $P = 0.002$–0.003) during the [VFT + post-VFT] period. The [oxy-Hb] changes in the ADHD group were significantly smaller than those recorded in the HC group in 2 channels corresponding to the left VLPFC and DLPFC (ch13 and 34; post-hoc $P = 0.004$–0.019) during the [VFT + post-VFT] period.

3.3. Classification and cross-validation

3.3.1. Discrimination between the ASDs and ADHD groups

ANOVA revealed the presence of significant differences between patients with ASDs and those with ADHD in the left VLPFC. Individual brain responses were characterized by expression values in 2 channels with significant differences in the mean [oxy-Hb] during the SST period between ASDs and ADHD adults (ch50 and 51). The stepwise analysis selected 1 channel (ch50: left VLPFC) using the mean [oxy-Hb] during the SST period ($P = 0.02$). The leave-one-out classification algorithm using the mean [oxy-Hb] during the SST period had an accuracy of 72.9% (sensitivity, 85.7%; specificity, 57.9%).

Individual brain responses were characterized by expression values in 5 channels with significant differences in the mean [oxy-Hb] during the [SST + post-SST] period between adults with ASDs and those with ADHD (ch24, 30, 41, 50, and 51). The stepwise regression analysis selected 1 channel (ch30: left VLPFC) using the mean [oxy-Hb] during the [SST + post-SST] period ($P = 0.002$). The algorithm that used the mean [oxy-Hb] during the [SST + post-SST] period had high accuracy (81.4%; sensitivity, 90.0%; specificity, 70.6%).

3.3.2. Discrimination of the ASDs from the HC group

ANOVA revealed the presence of significant differences between patients with ASDs and HC individuals in the broad prefrontal area. Individual brain responses were characterized by expression values in 34 channels that were significantly different regarding the mean [oxy-Hb] during the SST period between patients with ASDs and healthy adults (ch2, 3, 7–13, 17, 18, 20, 22, 24, 28, 29, 31, 32, 35–39, 41, 42, and 45–52). The stepwise regression analysis selected 1 channel (ch39: left VLPFC) using the mean [oxy-Hb] during the SST period ($P < 0.001$). The leave-one-out classification algorithm had an accuracy of 81.1%

(sensitivity, 90.5%; specificity, 71.4%) using the mean [oxy-Hb] during the SST period.

Individual brain responses were characterized by expression values in 36 channels that showed significant differences in the mean [oxy-Hb] during the [SST + post-SST] period between patients with ASDs and healthy adults (ch2, 3, 7–10, 12, 13, 18–20, 24–32, 35–39, 41, 42, and 45–52). The stepwise regression analysis selected 2 channels (ch47 and 50: frontal pole and left VLPFC) using the mean [oxy-Hb] during the [SST + post-SST] period ($P < 0.001$). The algorithm that used the mean [oxy-Hb] during the [SST + post-SST] period had high accuracy (89%; sensitivity, 90.0%; specificity, 80.0%).

3.3.3. Discrimination of the ADHD from the HC group

ANOVA revealed the presence of significant differences between patients with ADHD and HC individuals in the right pre-SMA, right PMA, and bilateral DLPFC. Individual brain responses were characterized by expression values in 17 channels with significant differences in the mean [oxy-Hb] during the SST period between patients with ADHD and healthy adults (ch1–3, 11–13, 18, 22, 28, 29, 36, 38, 39, and 46–49). The stepwise regression analysis selected 1 channel (ch11: right pre-SMA and right PMA) using the mean [oxy-Hb] during the SST period. The leave-one-out classification algorithm using the mean [oxy-Hb] during the SST period had a mean accuracy of 78.8% (sensitivity, 84.2%; specificity, 76.2%).

Individual brain responses were characterized by expression values in 11 channels with significant differences in the mean [oxy-Hb] during the [SST + post-SST] period between patients with ADHD and healthy adults (ch3, 13, 27, 28, 35, 38, 39, and 46–49).

The stepwise regression analysis selected 1 channel (ch13: right pre-SMA and right PMA) using the mean [oxy-Hb] during the [SST+post-SST] period ($P = 0.006$). The algorithm that used the mean [oxy-Hb] during the [SST + post-SST] period had a mean accuracy of 72.5% (sensitivity, 72.2%; specificity, 71.4%).

3.3.4. Additional analyses

There were no significant main effects in the results obtained for [deoxy-Hb] during the task or the [task + post-task] period, for either the SST or VFT tasks (see inline Supplementary material A. 2). In addition, the secondary group comparison (the ASDs subgroup with ADHD symptoms, the entire ADHD group, and the entire HC group) yielded statistical conclusions regarding clinical characteristics, behavioral results, and NIRS data results that were similar to those of the original group comparisons (see Inline Supplementary Table S3 and Supplementary material A. 3). There were no significant differences in NIRS data between male and female subjects during the task or the [task + post-task] period. Finally, for both the SST and VFT, there were no significant correlations between [oxy-Hb] changes during the task or the [task + post-task] period and clinical symptoms or task performance for either the ASDs or the ADHD group.

Inline Supplementary Table S3 can be found online at http://dx.doi.org/10.1016/j.nicl.2013.10.002.

4. Discussion

To our knowledge, this is the first study showing differences in prefrontal activation associated with inhibitory control between adults with ASDs and those with ADHD. We found more profound abnormalities in the PFC during inhibitory control in drug-naïve individuals with ASDs than in drug-naïve individuals with ADHD, despite similar performance levels. Although the ASDs group showed underactivation in the left VLPFC compared to the HC group, the ADHD group did not exhibit a significant decrease in VLPFC activation compared to the HC group. Significant differences between the ASDs and ADHD groups were found during the SST, even in comparisons between the ASDs subgroup with ADHD symptoms and the ADHD group. These differences in activation were localized to the left VLPFC. In contrast, there were no significant differences in [oxy-Hb] increases during the VFT between the ASDs and ADHD groups. The use of NIRS, a portable neuroimaging device, represented a strong advantage of our study. Therefore, our findings may be a step toward the development of a clinically useful biomarker for the differential diagnosis of the 2 commonest neurodevelopmental disorders, which has been difficult when based on clinical and neuropsychological measures.

4.1. Activation of [Oxy-Hb] in the left VLPFC

This study found significantly reduced activation in the left VLPFC in drug-naïve adults with ASDs compared to drug-naïve adults with ADHD (Figs. 4 and 5), which is consistent with the previously reported structural abnormalities in the left VLPFC of patients with ASDs, including reduced gray matter density (Yamasaki et al., 2010; Abell et al., 1999). The right dominant abnormalities observed in the ADHD group were consistent with the results of previous structural (Makris et al., 2007; Overmeyer et al., 2001) and fMRI studies performed during go/no-go (Casey et al., 2007) and stop tasks (Rubia et al., 1999; Hart et al., 2013). Our findings are also consistent with the results of fMRI studies showing dysfunction in this region during facial imitation (Dapretto et al., 2006; Bookheimer et al., 2008). Action mirroring is assumed to underlie the imitation of an observed action, social understanding, and communication with other people, and the mirroring system is a function of the VLPFC (Dapretto et al., 2006).

The reduced [oxy-Hb] increase observed in the left VLPFC of the ASDs group was inconsistent with the results of previous studies showing increased activation (Schmitz et al., 2006) or similar activation (Xiao et al., 2012) in this region for the ASDs group compared to that for the HC group during a go/no-go task. Thus, the SST load, as an inhibition task, may be higher than that of the go/no-go task (Rubia et al., 2001).

Furthermore, our previous study using NIRS during a go/no-go task found that activation under the no-go condition was lower than that under the go condition in the HC group (Nishimura et al., 2011), unlike the results of the present study. Therefore, the pattern of activation observed in the PFC during the SST may be different from that observed in a go/no-go task. The present results for the SST showed that the ASDs group might have a greater abnormality in the left VLPFC than the ADHD group. This result is consistent with the findings of a neuropsychological study reporting that children with ASDs had a more profound disability in inhibitory control than did children with ADHD (Corbett et al., 2009). An fMRI study performed in children showed that the DLPFC was significantly less activated in boys with ADHD than in those with ASDs during a sustained attention task (Christakou et al., 2012), which is in contrast with the activation pattern observed here. This might be because the task used in that study did not involve inhibitory controls.

The meaning of the [oxy-Hb] reascending observed in the left VLPFC in the ADHD group during the post-SST period remains unclear. However, patients with schizophrenia also showed a similarly robust [oxy-Hb] reascending during the post-task period of the VFT in previous NIRS studies (Suto et al., 2004; Takizawa et al., 2008). These results may be explained by a common dysfunction of the monoamine system in ADHD and schizophrenia, as the repertoire of ADHD-related genes resembles that of schizophrenia-related genes (Williams et al., 2010b; Burbach, 2010). In the present study, NIRS signal analyses that included the post-SST period distinguished the ASDs and ADHD groups better (Fig. 5). The classification accuracy observed between the ASDs and ADHD groups using [oxy-Hb] changes during the [SST + post-SST] period was also higher than the accuracy obtained using [oxy-Hb] changes only during the SST period. The high time resolution of NIRS enables detailed measurements of time-course changes, thus providing important insights into differences in inhibitory control during the SST between patients with ASDs and those with ADHD.